STATISTICS, OPTIMIZATION AND INFORMATION COMPUTING
Stat., Optim. Inf. Comput., Vol. **16**, October 2026, pp 3637–3668.
Published online in International Academic Press (www.IAPress.org)

A Fractional-Order Caputo SEICRD Model for Evaluating Non-Pharmaceutical Interventions in COVID-19 Transmission Dynamics in South Africa

Mawada Ali [1], Mohamed Bakheet [1], H.Elfakie [2,3], Eihab Bashier [4,5,*]

[1] *Department of Mathematical Modelling, Al-Neelain University, Sudan*
[2] *Department of Mathematics and Computer Science, International University of Africa, Sudan*
[3] *Department of Mathematics and Statistics, Kampala International University, Uganda*
[4] *Faculty of Education and Arts, Sohar University, Sohar, Oman*
[5] *Department of Applied Mathematics, University of Khartoum, Sudan*

Abstract The COVID-19 pandemic has had a significant impact on South Africa, motivating the development of reliable mathematical models to evaluate intervention strategies. In this paper, a fractional-order SEICRD model based on the Caputo derivative is proposed to describe the transmission dynamics of COVID-19 and to assess the effects of non-pharmaceutical interventions. Memory effects are incorporated through the fractional-order formulation, while a time-dependent infectious communication rate is modeled using the Woods-Saxon function to mathematically represent the continuous shifts in transmission rates resulting from evolving public health policies. The basic reproduction number and the effective reproduction number are derived, and model parameters, including the fractional order, are estimated using reported daily cases, daily recovered cases, and ICU data from May 26, 2020, to March 20, 2021, covering the first and second epidemic waves. Sensitivity analysis is performed to identify the most influential parameters. The fractional-order model fits the observed infected and ICU data at least as well as its integer-order counterpart while parsimoniously capturing memory effects in transmission; a profile analysis indicates that the fractional order itself is only weakly identified, and the model's adequacy is supported by residual diagnostics and a random hold-out test. Numerical simulations indicate that non-pharmaceutical interventions, such as lockdowns and reduced contact rates, play a crucial role in controlling disease spread. Translating the fitted ICU trajectories into operational terms, the memory-driven dynamics correspond to a saving of roughly 125,000 ICU bed-days relative to the integer-order projection, and initiating contact-reduction measures 7–10 days ahead of a turning point substantially lowers peak ICU demand. The results highlight the importance of early implementation and sustained control measures in mitigating COVID-19 transmission in South Africa.

Keywords Fractional-order model, Caputo derivative, COVID-19, Non-pharmaceutical interventions, Sensitivity analysis, Effective reproduction number

AMS 2010 subject classifications 34A08, 92D30, 34D20

DOI: 10.19139/soic-2310-5070-3525

1. Introduction

Coronavirus disease (COVID-19) is an infectious respiratory illness caused by the novel coronavirus SARS-CoV-2, which emerged in Wuhan, China, in late 2019 and rapidly developed into a global pandemic [1]. Coronaviruses constitute a large family of viruses responsible for respiratory infections ranging from mild illnesses to severe diseases such as Severe Acute Respiratory Syndrome (SARS) and Middle East Respiratory Syndrome (MERS) [2]. COVID-19 is primarily transmitted through respiratory droplets and close contact, with increasing evidence

*Correspondence to: Eihab Bashier (Email: ebashier@su.edu.om), Department of Mathematics, Faculty of Education and Arts, Sohar University, Oman.

ISSN 2310-5070 (online) ISSN 2311-004X (print)

supporting airborne transmission in crowded and poorly ventilated environments [3]. Common symptoms include fever, dry cough, fatigue, and shortness of breath, while severe complications occur more frequently among older adults and individuals with underlying health conditions [4]. In addition, the ability of the virus to survive on surfaces for extended periods has contributed to indirect transmission [5]. During the early stages of the pandemic, the absence of effective pharmaceutical treatments led to the widespread adoption of non-pharmaceutical interventions such as social distancing, mask usage, testing, isolation, and lockdown measures.

Within this global framework, South Africa has faced considerable epidemiological and socio-economic challenges since the confirmation of its first COVID-19 case in March 2020. The country experienced multiple epidemic waves of varying intensity, resulting in the implementation of strict public health measures, including nationwide lockdowns, travel restrictions, and mandatory mask policies. Despite these interventions, the healthcare system experienced significant pressure, particularly during peak infection periods. Notably, South Africa contributed to the global understanding of COVID-19 through the identification of new variants, especially the Beta variant, emphasizing the importance of continuous surveillance and adaptive modeling approaches. By early 2021, cumulative COVID-19-related deaths had exceeded 30,000, highlighting the urgent need for robust mathematical models capable of capturing complex transmission dynamics and evaluating the long-term impact of intervention strategies.

Mathematical modeling has therefore played a central role in analyzing the spread and control of COVID-19. In recent years, fractional-order models have emerged as powerful tools for studying infectious diseases. Unlike classical deterministic models, fractional-order models incorporate memory effects, whereby the current state of the epidemic depends on both present conditions and past dynamics [6, 7, 8]. This property enhances model realism, as infection transmission and population responses are influenced by previous exposures, delayed immunity, and gradual behavioral changes. In contrast, classical deterministic models assume instantaneous changes based solely on current states, which may limit their ability to capture complex epidemic behavior [7, 9].

The COVID-19 pandemic exhibits pronounced nonlocal and non-instantaneous dynamics due to incubation periods, delayed symptom onset, behavioral responses to public health measures, and immunity accumulated from previous infection waves [10, 8]. These features are particularly relevant when analyzing consecutive epidemic waves, where the second wave is strongly influenced by residual infections, immunity, and behavioral changes from the first wave. Fractional-order models address these challenges by incorporating memory and hereditary effects, providing a more comprehensive description of epidemic dynamics [11, 12].

Several studies have demonstrated the effectiveness of fractional-order models in COVID-19 analysis. Tuan et al. [6] examined equilibrium points and reproduction numbers using a Caputo fractional-order model, showing epidemic persistence when the reproduction number exceeds unity. Atangana [13] investigated the impact of lockdown and social distancing measures and demonstrated their potential to significantly reduce transmission. Ahmad et al. [7] validated fractional compartmental models using real data and confirmed the stability of predictor–corrector numerical schemes. Additional studies addressed super-spreaders [9], parameter estimation in multi-compartment models [10], multiple virus variants [8], and fractional uncertain differential equations for improved forecasting [11]. Comprehensive reviews of fractional epidemic models were provided in [12].

Despite these advances, most existing studies focus on either general theoretical modeling or the analysis of a single epidemic wave, often failing to account for the cumulative impact of consecutive waves in complex settings. The present study bridges this gap by developing a comprehensive fractional-order framework that integrates memory effects–via the Caputo derivative–with the dynamics of multiple successive COVID-19 waves in South Africa. Unlike earlier works, we employ the Woods–Saxon function to model the time–dependent transmission rate, which allows for a more nuanced representation of shifting public health interventions and societal responses over time. This approach does not merely extend our previous deterministic work, it provides a robust analytical tool that captures the interplay between historical infection states and current epidemic trajectories, thereby offering a more accurate and realistic assessment of transmission dynamics in environments characterized by volatile policy changes. The main objectives of this study are to capture long-term memory effects in COVID-19 transmission, evaluate the impact of non-pharmaceutical interventions, and provide insights to support effective epidemic control strategies. The proposed model extends a previously published deterministic model [14] by incorporating the Caputo fractional derivative to account for memory and hereditary effects. When the fractional order $\eta = 1$, the

model reduces to the classical deterministic formulation, allowing a clear comparison between fractional- and integer-order dynamics. The remainder of this paper is organized as follows. Section 2 introduces the mathematical preliminaries of the Caputo fractional derivative. Section 3 presents the proposed SEICRD fractional-order model. Section 4 discusses the equilibrium points and stability analysis. Section 5 addresses the existence and uniqueness of solutions. Section 6 presents the numerical scheme, the data sources, and the parameter-estimation methodology. Section 7 reports the estimated parameters and their epidemiological interpretation, the sensitivity analysis, the scenario simulations, the fractional-versus-integer model comparison, the model validation, and the public-health implications. Section 8 discusses the limitations of the study. Finally, Section 9 concludes the paper with key findings and implications.

2. Preliminaries for Caputo fractional derivative

In this section, we recall some of the fundamental concepts of fractional differential calculus. We introduce types of fractional derivatives and fractional integrals, the first of which is the Caputo derivative.

Definition 2.1
[15] The fractional derivative of $f(x)$ in the Caputo sense is defined as

$$^{C}D_x^{\eta} f(x) = I_x^{n-\eta} f^{(n)}(x) = \frac{1}{\Gamma(n-\eta)} \int_0^x \frac{f^{(n)}(x)}{(x-v)^{n-\eta-1}} dv, (n-1) \leq \eta < n$$

where n is integer and η is real number. Here, I_x^{η} is the Riemann-Liouville integral operator of order $\eta \in (0,1)$ Also, the corresponding fractional integral of order η with $\Re(\eta) > 0$ is given by

$$^{C}I_x^{\eta} f(x) \quad = \quad \frac{1}{\Gamma(\eta)} \int_0^x (x-v)^{\eta-1} f(v) dv \tag{1}$$

This definition is widely used in modeling real systems because it allows the use of standard initial conditions, just like in ordinary differential equations.

Definition 2.2
[16] The Laplace transform of the Caputo fractional derivative operator of order η is defined as

$$L[^{C}D_x^{\eta} f(x)](s) = s^{\eta} Lf(x) - \sum_{i=0}^{n-1} s^{\eta-i-1} f^{(i)}(0), n-1 < \eta \leq n \in N$$

Definition 2.3
Mittag-Leffler function
The function $E_{\eta}(z)$ defined by [17]

$$E_{\eta}(z) = \sum_{k=0}^{\infty} \frac{z^k}{\Gamma(\eta k+1)}, \; E_{\eta,\beta}(z) = \sum_{k=0}^{\infty} \frac{z^k}{\Gamma(\eta k+\beta)}, \; (z \in C, Re(\eta) > 0)$$

The Laplace transform of the Mittag-Leffler function defined by

$$L^{-1}[\frac{s^{\eta-\beta}}{s^{\eta}-\lambda}] \quad = \quad z^{\beta-1} E_{\eta,\beta}(\lambda z^{\eta}) \tag{2}$$

Recurrence relation of $E_{\eta,\beta}(z)$

$$E_{\eta,\beta}(z) = z E_{\eta,\eta+\beta}(z) + \frac{1}{\Gamma(\beta)} \tag{3}$$

Theorem 2.4
$k(x,t,y), f(x)$ be continuous function of their argument $a \leq x, t \leq b, -\infty < y < \infty$, and suppose the satisfies that it Lipschitz condition in y [18]

$$|k(x,t,y_2) - k(x,t,y_1)| \leq A|y_2 - y_1|$$

Definition 2.5
The method of successive approximations, In this method, we replace the unknown function $y(x)$ under the integral sign of the Volterra equation

$$y(x) = \lambda \int_a^b k(x,t,y(t))dt + f(x)$$

The method of successive approximations

$$y_{n+1}(x) = \lambda \int_a^b k(x,t,y_n(t))dt + f(x), n = 0,1,2,...$$

with an arbitrary continuous function $y_0(x)$[18]

3. A mathematical model using the Caputo fractional derivative

We consider an SEICRD epidemic model, where the total active human population at any time t is denoted by $N(t) = S(t) + E(t) + I(t) + C(t) + R(t)$, which is divided into five active compartments: Susceptible individuals $S(t)$, Exposed $E(t)$, Infected individuals $I(t)$, individuals in the Intensive Care Unit (ICU) $C(t)$, and Recovered individuals $R(t)$. Additionally, the compartment $D(t)$ tracks the cumulative number of dead individuals who died due to the coronavirus. Given the short time frame of the pandemic under study, natural birth and death rates are neglected. The disease transmission occurs from $S(t)$ to $E(t)$ at the rate $\frac{\gamma\,\beta(t)\,S(t)\,I(t)}{N}$ for infection transmission, and progression from $E(t)$ to $I(t)$ occurs at rate σ. Recovery and transition to critical cases occur from $I(t)$ at rates $\delta\alpha$ and $\delta(1-\alpha)$, respectively, and finally, individuals in the ICU either recover at rate $\lambda ordieduetothediseaseatrate\mu$. The time-dependent infectious communication rate $\beta(t)$, representing the impact of public health interventions and control policies in South Africa, is modeled through the Woods–Saxon function [19]. characterized by fitting parameters $a_0, Z, t_{\text{Turning}}$,and b_{Duration}, which describe the smooth reduction in infection contact rate over time.
In this model, the infectious communication rate $\beta(t)$ is introduced as a time-dependent parameter to capture the impact of public health interventions and state policies implemented in South Africa. The temporal variation of $\beta(t)$ is modeled using the Woods–Saxon function [19], which is mathematically designed to describe and characterize transitions in terms of their scale (strength), smoothness or abruptness, thickness (duration), and tipping point. The parameters $a_0, Z, t_{\text{Turning}}, b_{\text{Duration}}$ are fitting parameters that describe the reduction in the rate of infectious contacts over time. The Woods–Saxon function is particularly suitable for representing the effects of public health interventions and government policies, as it allows for smooth temporal transitions in the infectious communication rate. To account for the presence of two epidemic waves, the function is extended to include two transition peaks, enabling the modified $\beta(t)$ to represent both waves within a single formulation. This approach provides a realistic description of changes in transmission intensity resulting from variations in intervention measures, population behavior, and epidemic conditions. Thus, the active living population size is given by:

$$N(t) = S(t) + E(t) + I(t) + C(t) + R(t).$$

The dynamics of COVID-19 transmission within the population are described by the following system of deterministic nonlinear differential equations.

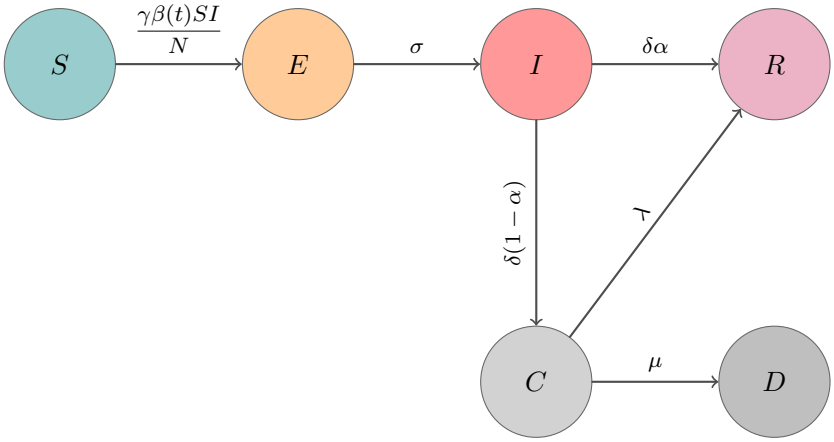

Figure 1. Schematic diagram of the proposed fractional-order SEICRD model.

Model Diagram

$$\begin{aligned}
\frac{dS}{dt} &= -\frac{\gamma\,\beta(t)\,S(t)\,I(t)}{N} \\
\frac{dE}{dt} &= \frac{\gamma\,\beta(t)\,S(t)\,I(t)}{N} - \sigma E(t) \\
\frac{dI}{dt} &= \sigma\,E(t) - \delta\,I(t) \\
\frac{dC}{dt} &= \delta\,(1-\alpha)I(t) - (\mu+\lambda)\,C(t) \\
\frac{dR}{dt} &= \delta\,\alpha\,I(t) + \lambda\,C(t) \\
\frac{dD}{dt} &= \mu\,C(t)
\end{aligned} \tag{4}$$

where $\beta(t)$ is given by

$$\beta(t) = a_0\left(1 + \frac{Z_1}{1+\exp\left((t-t_{\text{Turning}_1})/b_{\text{Duration}_1}\right)} + \frac{Z_2}{1+\exp\left((t-t_{\text{Turning}_2})/b_{\text{Duration}_2}\right)}\right)$$

subject to the initial conditions:

$$S(0) = S_0 \geq 0, E(0) = E_0 \geq 0, I(0) = I_0 \geq 0, C(0) = C_0 \geq 0, R(0) = R_0 \geq 0, D(0) = D_0 \geq 0.$$

By replacing the first-order differential derivatives in System (4) with Caputo fractional derivatives, we obtain the following fractional-order SEICRD model for COVID-19 transmission for $t > 0$ and $\eta \in (0,1)$ is given by

$$\begin{aligned}
{}^{C}D_t^{\eta}S(t) &= -\frac{\gamma\,\beta(t)\,S(t)\,I(t)}{N} \\
{}^{C}D_t^{\eta}E(t) &= \frac{\gamma\,\beta(t)S(t)\,I(t)}{N} - \sigma E(t) \\
{}^{C}D_t^{\eta}I(t) &= \sigma\,E(t) - \delta\,I(t) \\
{}^{C}D_t^{\eta}C(t) &= \delta\,(1-\alpha)I(t) - (\mu+\lambda)\,C(t) \\
{}^{C}D_t^{\eta}R(t) &= \delta\,\alpha\,I(t) + \lambda\,C(t) \\
{}^{C}D_t^{\eta}D(t) &= \mu\,C(t)
\end{aligned} \tag{5}$$

Table 1. Description Parameters in the model

parameters	Descriptions
N	The total population
γ	Effective transmission rate
β	infectious communication rate or Hazard rate of infection
σ	The incubation rate
δ	The estimated duration or illness
α	Recovery rate without being in ICU
λ	Recovery rate of ICU patient
μ	Death rate due to disease Covid-19 for individuals in the C(t)

where initial conditions are

$$S(0) = S_0, E(0) = E_0, I(0) = I_0, C(0) = C_0\,, R(0) = R_0, D(0) = D_0.$$

Vital dynamics and the constant-population reduction. System (5) treats the living population $N(t) = S(t) + E(t) + I(t) + C(t) + R(t)$ as closed. To make the demographic bookkeeping of a model that already contains disease-induced mortality explicit, we consider the corresponding open system in which susceptibles are recruited at the per-capita birth rate b and every living compartment is subject to the natural (non-COVID) mortality rate d:

$$\begin{aligned}
{}^{C}D_t^{\eta} S(t) &= b\,N(t) - \frac{\gamma\,\beta(t)\,S(t)I(t)}{N(t)} - d\,S(t)\\
{}^{C}D_t^{\eta} E(t) &= \frac{\gamma\,\beta(t)\,S(t)I(t)}{N(t)} - \sigma E(t) - d\,E(t)\\
{}^{C}D_t^{\eta} I(t) &= \sigma E(t) - \delta I(t) - d\,I(t)\\
{}^{C}D_t^{\eta} C(t) &= \delta(1-\alpha) I(t) - (\mu+\lambda) C(t) - d\,C(t)\\
{}^{C}D_t^{\eta} R(t) &= \delta\alpha I(t) + \lambda C(t) - d\,R(t)\\
{}^{C}D_t^{\eta} D(t) &= \mu\,C(t)
\end{aligned} \tag{6}$$

Migration and immigration are omitted, which is justified by the border closures and movement restrictions in force during the study period. The demographic rates are obtained from World Health Organization estimates for South Africa: a total life expectancy of 61.5 years gives a natural mortality rate $d = 1/(61.5 \times 365) \approx 4.45 \times 10^{-5}\ \mathrm{day}^{-1}$, and an annual population growth rate of 1.3% gives a birth rate $b = 0.013/365 + d \approx 8.02 \times 10^{-5}\ \mathrm{day}^{-1}$ (the net growth rate being $b - d$). Because the data are daily, both rates are expressed per day rather than per year.

These daily demographic rates are roughly four orders of magnitude smaller than the epidemiological rates ($\sigma, \delta \sim 10^{-1}\ \mathrm{day}^{-1}$), so over the finite study horizon their effect is small. Integrating (6) at the estimated parameters changes the infected, ICU, and recovered trajectories by less than 1% relative to the closed system (5) (0.59%, 0.66%, and 1.0% in I, C, and R, respectively), the living population grows by under 1%, and the overall goodness-of-fit is essentially unchanged (RMSE 2827.3 versus 2833.6). We therefore carry out the equilibrium and stability analysis of Section 4 and the parameter estimation of Section 7 on the reduced system (5) (formally $b = d = 0$), understanding (6) as the demographically complete formulation and the constant-population reduction as an approximation whose error over the interval considered is below one percent.

4. Dynamics of the fractional-order model

4.1. Positivity and boundedness

Let $N(t) = S(t) + E(t) + I(t) + C(t) + R(t)$ represent the total active (living) population at time t. The compartment $D(t)$ denotes the cumulative number of deaths due to the disease and is excluded from the active population interacting in the system.

Consider the feasible region:

$$\Phi = \left\{(S, E, I, C, R, D) \in \mathcal{R}_6^+ : S + E + I + C + R \leq N(0), \text{ and } D \leq N(0)\right\}.$$

We show that the closed set Φ represents the region of mathematical and epidemiological persistence for system (5).

Lemma 4.1
The closed set Φ is positively invariant with respect to the system (5).

Proof
By summing the first five equations of system (5), the Caputo fractional derivative of the active population $N(t)$ satisfies:

$$^{C}D_t^{\eta} N(t) = -\mu C(t).$$

Since all state variables remain non-negative in $\mathcal{R}_6^+$, it follows that:

$$^{C}D_t^{\eta} N(t) \leq 0.$$

Applying the Laplace transform to both sides yields:

$$s^{\eta} N(s) - s^{\eta-1} N(0) \leq 0,$$

which can be rewritten as:

$$N(s) \leq \frac{N(0)}{s}.$$

Taking the inverse Laplace transform, we obtain:

$$N(t) \leq N(0) \quad \text{for all } t \geq 0.$$

Furthermore, since $^{C}D_t^{\eta} D(t) = \mu C(t)$, it is clear that $^{C}D_t^{\eta}(N(t) + D(t)) = 0$, which yields $N(t) + D(t) = N(0) + D(0)$. Given that $N(t) \geq 0$, it directly follows that $D(t) \leq N(0) + D(0)$. Assuming $D(0) = 0$, we get $D(t) \leq N(0)$. Hence, the closed set Φ is positively invariant with respect to the model (5). □

Theorem 4.2
The solution of the system (5) is non-negative, bounded for all

$$\{S(0), E(0), I(0), C(0), R(0), D(0) \in \mathbb{R}_+^6\}$$

, and also defined for all $t > 0$.

Proof
Consider the equations of system (5), substitute

$$S = 0, E = 0, I = 0, C = 0, R = 0, D = 0$$

in the first, second, third, fourth, fifth, and Sixth equations, respectively. Then we have

$$\begin{aligned}
{}^{C}D_t^{\eta} S(t)\big|_{S\to 0} &= 0 \\
{}^{C}D_t^{\eta} E(t)\big|_{E\to 0} &= \frac{\gamma\,\beta(t)\,S\,I}{N} > 0 \\
{}^{C}D_t^{\eta} I(t)\big|_{I\to 0} &= \sigma\,E > 0 \\
{}^{C}D_t^{\eta} C(t)\big|_{I\to 0} &= \delta(1-\alpha)\,I > 0 \\
{}^{C}D_t^{\eta} R(t)\big|_{R\to 0} &= \delta\alpha\,I + \lambda^{1-\eta}\,\lambda\,C > 0 \\
{}^{C}D_t^{\eta} D(t)\big|_{D\to 0} &= \mu\,C > 0
\end{aligned} \tag{7}$$

Positive invariant region that meets the model (5) is given by

$$\Phi = \{(S(t), E(t), I(t), C(t), R(t), D(t) \in \mathbb{R}_+^6 : N(t) \le N(0), \forall t \ge 0\}$$

□

4.2. Disease-Free Equilibrium

The coordinates of the disease-free equilibrium point (S, E, I, C, R, D) the fractional order system (5), obtained by the following equations

$${}^{C}D_t^{\eta} S(t) = {}^{C}D_t^{\eta} E(t) = {}^{C}D_t^{\eta} I(t) = {}^{C}D_t^{\eta} C(t) = {}^{C}D_t^{\eta} R(t) = 0,\ {}^{C}D_t^{\eta} D(t) = 0$$

Therefore, the system of equations has a disease-free equilibrium, denoted by E_{dfe}, i.e.,

$$E_{dfe} = (S_0, E_0, I_0, C_0, R_0, D_0) = (N, 0, 0, 0, 0, 0)$$

4.3. The basic reproduction number

Based on the system of equation (5), we have three infected classes $I(t)$, $E(t)$, $C(t)$.

$$\begin{aligned}
{}^{C}D_t^{\eta} E(t) &= \frac{\gamma\,\beta(t)\,S(t)\,I(t)}{N} - \sigma E(t) \\
{}^{C}D_t^{\eta} I(t) &= \sigma\,E(t) - \delta\,I(t) \\
{}^{C}D_t^{\eta} C(t) &= \delta\,(1-\alpha) I(t) - (\mu+\lambda)\,C(t)
\end{aligned}$$

Following the next-generation matrix approach [20], we first rewrite the system as

$${}^{C}D_t^{\eta} x(t) = F(x(t)) - V(x(t)), \quad \text{where } x = [E, I, C]^T$$

where

$$f(x) = \begin{bmatrix} \frac{\gamma\,\beta(t)\,S(t)\,I(t)}{N} \\ 0 \\ 0 \end{bmatrix}, v(x) = \begin{bmatrix} \sigma E(t) \\ \sigma E(t) + \delta I(t) \\ \delta(1-\alpha) I(t) + (\mu+\lambda) C(t) \end{bmatrix} \tag{8}$$

Now the Jacobian of $f(x)$ and $v(x)$ of the disease free equilibrium point is

$$F = \begin{bmatrix} 0 & \gamma\,\beta_0 & 0 \\ 0 & 0 & 0 \\ 0 & 0 & 0 \end{bmatrix} \tag{9}$$

$$V = \begin{bmatrix} \sigma & 0 & 0 \\ -\sigma & \delta & 0 \\ 0 & -(1-\alpha)\delta & \mu+\lambda \end{bmatrix} \tag{10}$$

Therefore

$$V^{-1} = \begin{bmatrix} \frac{1}{\sigma} & 0 & 0 \\ \frac{1}{\delta} & \frac{1}{\delta} & 0 \\ \frac{(1-\alpha)}{(\mu+\lambda)} & \frac{(1-\alpha)}{(\mu+\lambda)} & \frac{1}{\mu+\lambda} \end{bmatrix} \tag{11}$$

The reproduction number of the system equation (5) is as follows

$$\mathcal{R}_0 = \rho(FV^{-1}) \tag{12}$$

Therefore

$$FV^{-1} = \begin{bmatrix} \frac{\gamma\,\beta_0}{\delta} & \frac{\gamma\,\beta_0}{\delta} & 0 \\ 0 & 0 & 0 \\ 0 & 0 & 0 \end{bmatrix} \tag{13}$$

The eigenvalues of FV^{-1} are

$$(\frac{\gamma\,\beta_0}{\delta}, 0, 0) \tag{14}$$

Thus

$$\mathcal{R}_0 = \rho(FV^{-1}) \quad = \quad \frac{\gamma\,\beta_0}{\delta} \tag{15}$$

and the effective reproduction number is given by

$$R_{eff} \quad = \quad \frac{\gamma\,\beta(t)\,S(t)}{\delta\,N} \tag{16}$$

4.4. Endemic equilibrium

Theorem 4.3
For the system of equation (5), there exists a unique positive endemic equilibrium point E^*_{en} if $\mathcal{R}_0 > 1$.

Proof
An endemic equilibrium $E^*_{en} = (S^*, E^*, I^*, C^*, R^*, D^*)$, with $S^*, E^*, I^*, C^*, R^*, D^* > 0$ satisfies

$$S^* \quad = \quad \frac{\delta N}{\gamma\,\beta^*} \tag{17}$$

$$E^* \quad = \quad N\left[1 - \frac{\delta}{\gamma\,\beta^*}\right]\left[\frac{\delta\,(\mu+\lambda)}{A}\right] \tag{18}$$

$$I^* \quad = \quad N\left[1 - \frac{\delta}{\gamma\,\beta^*}\right]\left[\frac{\sigma\,(\mu+\lambda)}{A}\right] \tag{19}$$

$$C^* \quad = \quad N\left[1 - \frac{\delta}{\gamma\,\beta^*}\right]\left[\frac{\sigma\,\delta\,(1-\alpha)}{A}\right] \tag{20}$$

$$R^* \quad = \quad N\left[1 - \frac{\delta}{\gamma\,\beta^*}\right]\left[\frac{\delta\,\sigma\,(\alpha(\mu+\lambda) - \lambda(1-\alpha)\,)}{A}\right] \tag{21}$$

$$D^* \quad = \quad N\left[1 - \frac{\delta}{\gamma\,\beta^*}\right]\left[\frac{\delta\,\sigma\,\mu(1-\alpha)}{A}\right] \tag{22}$$

where

$$A = \sigma\,(\mu+\lambda) + \delta\,(\mu+\lambda)(\sigma\,\alpha+1) + \delta\,\sigma(1-\alpha)\,(1-\lambda+\mu) + (\mu+\lambda)\,(\sigma + \delta\,(1+\sigma\,\alpha)\,)$$

□

4.5. Stability analysis

Theorem 4.4
The system of equations (5) is locally stable at the disease-free equilibrium point E_{dfe} when $\mathcal{R}_0 < 1$, and it becomes unstable when $\mathcal{R}_0 > 1$.

Proof
The Jacobian matrix with respect to the system of equation (5) is given by:

$$J = \begin{bmatrix} -\frac{\gamma\,\beta(t)\,I}{N} & 0 & -\frac{\gamma\,\beta(t)\,S}{N} & 0 & 0 & 0 \\ \frac{\gamma\,\beta(t)\,I}{N} & -\sigma & \frac{\gamma\,\beta(t)\,S}{N} & 0 & 0 & 0 \\ 0 & \sigma & -\delta & 0 & 0 & 0 \\ 0 & 0 & \delta\,(1-\alpha) & -\mu-\lambda & 0 & 0 \\ 0 & 0 & \alpha\,\delta & \lambda & 0 & 0 \\ 0 & 0 & 0 & \mu & 0 & 0 \end{bmatrix} \tag{23}$$

At E_{dfe}, the Jacobian matrix becomes

$$J(E_{dfe}) = \begin{bmatrix} 0 & 0 & -\gamma\,\beta_0 & 0 & 0 & 0 \\ 0 & -\sigma & \gamma\,\beta_0 & 0 & 0 & 0 \\ 0 & \sigma & -\delta & 0 & 0 & 0 \\ 0 & 0 & \delta\,(1-\alpha) & -\mu-\lambda & 0 & 0 \\ 0 & 0 & \alpha\,\delta & \lambda & 0 & 0 \\ 0 & 0 & 0 & \mu & 0 & 0 \end{bmatrix} \tag{24}$$

Thus, we get the eigenvalues are

$$\omega_1 = 0, \omega_2 = 0, \omega_3 = 0, \omega_4 = -\mu - \lambda$$
$$\omega_5 = -\frac{(\delta+\sigma)}{2} + K$$
$$\omega_6 = -\frac{(\delta+\sigma)}{2} - K$$

where

$$K = \frac{1}{2}\sqrt{4\gamma\,\beta_0\sigma + \delta^2 - 2\delta\sigma + \sigma^2}$$

If $\frac{(\delta+\sigma)}{2} > K$, which implies $\omega_5 < 0$, then $\mathcal{R}_0 < 1$. Consequently, the system of equations (5) is locally asymptotically stable for $\mathcal{R}_0 < 1$. On the other hand, if $\frac{(\delta+\sigma)}{2} < K$, which implies $\omega_5 > 0$, then $\mathcal{R}_0 > 1$, and thus the system of equations (5) becomes unstable for $\mathcal{R}_0 > 1$. □

Theorem 4.5
The endemic equilibrium E^*_{en} of system (5) is locally asymptotically stable whenever $\mathcal{R}_0 > 1$.

Proof
The characteristic equation associated with the endemic equilibrium point E^*_{en} is given by

$$m^6 + (A_1 + A_2)m^5 + (A_3 + \delta\eta\lambda\mu A_2)m^4 + (A_3 + A_4)m^3 + A_2A_4m^2 = 0. \tag{25}$$

By factoring out m^2, we obtain

$$m^4 + (A_1 + A_2)m^3 + (A_3 + \delta\eta\lambda\mu A_2)m^2 + (A_3 + A_4)m + A_2A_4 = 0, \tag{26}$$

where

$$\begin{aligned} A_1 &= \mu + \lambda + \delta + \sigma, \\ A_2 &= \beta^* \left(1 - \frac{\beta_0}{\beta^* \mathcal{R}_0}\right) \left(\frac{\sigma(\mu + \lambda)}{A}\right), \\ A_3 &= \delta\lambda + \delta\mu + \sigma\lambda + \sigma\mu, \\ A_4 &= \delta\sigma. \end{aligned}$$

For $\mathcal{R}_0 > \frac{\beta_0}{\beta^*} > 1$, all coefficients satisfy $A_1 > 0$, $A_2 > 0$, $A_3 > 0$, and $A_4 > 0$. Moreover, the following Routh–Hurwitz conditions hold:

$$(A_1 + A_2)(A_3 + \delta\sigma\lambda\mu A_2) > (A_3 + A_4),$$

and

$$\big[(A_1 + A_2)(A_3 + \delta\sigma\lambda\mu A_2) - (A_3 + A_4)\big](A_3 + A_4) > (A_1 + A_2)A_2A_4.$$

Therefore, by the Routh–Hurwitz stability criterion [21], the endemic equilibrium E^*_{en} is locally asymptotically stable if and only if $\mathcal{R}_0 > \frac{\beta_0}{\beta^*} > 1$. □

5. Existence and Uniqueness of Solutions

In this section, we establish the existence and uniqueness of the solution to the fractional SEICRD model. This analysis is crucial as it ensures that the model is mathematically well-posed, providing a rigorous foundation for the numerical simulations and parameter estimations performed in the subsequent sections.

$$\begin{aligned} {}^{C}D_t^{\eta} S(t) &= G_1(t, S(t)) \\ {}^{C}D_t^{\eta} E(t) &= G_2(t, E(t)) \\ {}^{C}D_t^{\eta} I(t) &= G_3(t, I(t)) \\ {}^{C}D_t^{\eta} C(t) &= G_4(t, C(t)) \\ {}^{C}D_t^{\eta} R(t) &= G_5(t, R(t)) \\ {}^{C}D_t^{\eta} D(t) &= G_6(t, D(t)) \end{aligned} \tag{27}$$

By integrating both sides of (1) from 0 to t, we obtain

$$\begin{aligned} S(t) - S(0) &= \frac{1}{\Gamma(\eta)} \int_0^t (t - \tau)^{\eta - 1} G_1(\tau, S(\tau)) d\tau \\ E(t) - E(0) &= \frac{1}{\Gamma(\eta)} \int_0^t (t - \tau)^{\eta - 1} G_2(\tau, E(\tau)) d\tau \\ I(t) - I(0) &= \frac{1}{\Gamma(\eta)} \int_0^t (t - \tau)^{\eta - 1} G_3(\tau, I(\tau)) d\tau \\ C(t) - C(0) &= \frac{1}{\Gamma(\eta)} \int_0^t (t - \tau)^{\eta - 1} G_4(\tau, C(\tau)) d\tau \\ R(t) - R(0) &= \frac{1}{\Gamma(\eta)} \int_0^t (t - \tau)^{\eta - 1} G_5(\tau, R(\tau)) d\tau \\ D(t) - D(0) &= \frac{1}{\Gamma(\eta)} \int_0^t (t - \tau)^{\eta - 1} G_6(\tau, D(\tau)) d\tau \end{aligned} \tag{28}$$

We show that the kernels G_i, for $i = 1, 2, 3, 4, 5, 6$, satisfy the Lipschitz condition and are contractions.

Theorem 5.1
The kernels G_i, for $i = 1, 2, 3, 4, 5, 6$, satisfy the Lipschitz condition and are contractions if the following inequalities hold:

$$0 \leq \frac{\gamma\beta(t)}{N} l_1 < 1, \quad 0 \leq \sigma < 1, \quad 0 \leq \delta < 1, \quad 0 \leq \mu + \lambda < 1.$$

Proof
For S and S_1, we have

$$\begin{aligned} \|G_1(t,S) - G_1(t,S_1)\| &= \left\| -\frac{\gamma\beta(t)SI}{N} + \frac{\gamma\beta(t)S_1 I}{N} \right\| \\ &= \left\| -\frac{\gamma\beta(t)I}{N}(S - S_1) \right\| \\ &\leq \frac{\gamma\beta(t)}{N} \|I\| \, \|S - S_1\| \\ &\leq b_1 \|S - S_1\|, \quad b_1 = \frac{\gamma\beta(t)}{N} l_1 \end{aligned} \tag{29}$$

where $\|I\| \leq l_1$, so $I(t)$ is bounded. Hence, G_1 satisfies the Lipschitz condition, and if $0 \leq b_1 < 1$, G_1 is a contraction.
Similarly,we can show that

$$\|G_2(t,E) - G_2(t,E_1)\| \leq b_2 \|E - E_1\|, \quad b_2 = \sigma \tag{30}$$
$$\|G_3(t,I) - G_3(t,I_1)\| \leq b_3 \|I - I_1\|, \quad b_3 = \delta \tag{31}$$
$$\|G_4(t,C) - G_4(t,C_1)\| \leq b_4 \|C - C_1\|, \quad b_4 = \mu + \lambda \tag{32}$$
$$\|G_5(t,R) - G_5(t,R_1)\| \leq b_5 \|R - R_1\|, \quad b_5 = 0 \tag{33}$$
$$\|G_6(t,D) - G_6(t,D_1)\| \leq b_6 \|D - D_1\|, \quad b_6 = 0 \tag{34}$$

Thus, for G_i, $i = 2, 3, 4, 5, 6$, the Lipschitz condition is satisfied, and if $0 \leq b_i < 1$ for $i = 2, 3, 4, 5, 6$, then G_i are contractions. □

Remark 1: The constants $b_5 = 0$ and $b_6 = 0$ correspond to the Recovered (R) and Deceased (D) compartments. Biologically, these classes act as final sinks that do not drive new infections. Mathematically, the model kernels are independent of R and D, making their partial derivatives zero. This naturally justifies $b_5 = 0$ and $b_6 = 0$ without affecting the theoretical validity of the uniqueness proof. According to system (5),we consider the following recursive forms using the method of successive approximations:

$$H_{1m}(t) = S_m(t) - S_{m-1}(t) = \frac{1}{\Gamma(\eta)} \int_0^t \left(G_1(\tau, S_{m-1}) - G_1(\tau, S_{m-2})\right)(t-\tau)^{\eta-1} d\tau$$
$$H_{2m}(t) = E_m(t) - E_{m-1}(t) = \frac{1}{\Gamma(\eta)} \int_0^t \left(G_2(\tau, E_{m-1}) - G_2(\tau, E_{m-2})\right)(t-\tau)^{\eta-1} d\tau$$
$$H_{3m}(t) = I_m(t) - I_{m-1}(t) = \frac{1}{\Gamma(\eta)} \int_0^t \left(G_3(\tau, I_{m-1}) - G_3(\tau, I_{m-2})\right)(t-\tau)^{\eta-1} d\tau$$
$$H_{4m}(t) = C_m(t) - C_{m-1}(t) = \frac{1}{\Gamma(\eta)} \int_0^t \left(G_4(\tau, C_{m-1}) - G_4(\tau, C_{m-2})\right)(t-\tau)^{\eta-1} d\tau$$
$$H_{5m}(t) = R_m(t) - R_{m-1}(t) = \frac{1}{\Gamma(\eta)} \int_0^t \left(G_5(\tau, R_{m-1}) - G_5(\tau, R_{m-2})\right)(t-\tau)^{\eta-1} d\tau$$
$$H_{6m}(t) = D_m(t) - D_{m-1}(t) = \frac{1}{\Gamma(\eta)} \int_0^t \left(G_6(\tau, D_{m-1}) - G_6(\tau, D_{m-2})\right)(t-\tau)^{\eta-1} d\tau$$

with initial conditions

$$S_0(t) = S(0),\ E_0(t) = E(0),\ I_0(t) = I(0),\ C_0(t) = C(0),\ R_0(t) = R(0),\ D_0(t) = D(0).$$

Taking the norm of the first equation, we obtain

$$\begin{aligned} \|H_{1m}(t)\| &= \|S_m(t) - S_{m-1}(t)\| \\ &= \left\| \frac{1}{\Gamma(\eta)} \int_0^t (G_1(\tau, S_{m-1}) - G_1(\tau, S_{m-2}))(t-\tau)^{\eta-1} d\tau \right\| \\ &\leq \frac{b_1}{\Gamma(\eta)} \int_0^t \|S_{m-1} - S_{m-2}\| d\tau \leq \frac{b_1}{\Gamma(\eta)} \int_0^t \|H_{1(m-1)}(\tau)\| d\tau \end{aligned} \tag{35}$$

Similarly, we have

$$\begin{aligned} \|H_{2m}(t)\| &\leq \frac{b_2}{\Gamma(\eta)} \int_0^t \|H_{2(m-1)}(\tau)\| d\tau \\ \|H_{3m}(t)\| &\leq \frac{b_3}{\Gamma(\eta)} \int_0^t \|H_{3(m-1)}(\tau)\| d\tau \\ \|H_{4m}(t)\| &\leq \frac{b_4}{\Gamma(\eta)} \int_0^t \|H_{4(m-1)}(\tau)\| d\tau \\ \|H_{5m}(t)\| &\leq \frac{b_5}{\Gamma(\eta)} \int_0^t \|H_{5(m-1)}(\tau)\| d\tau \\ \|H_{6m}(t)\| &\leq \frac{b_6}{\Gamma(\eta)} \int_0^t \|H_{6(m-1)}(\tau)\| d\tau \end{aligned} \tag{36}$$

Note that

$$H_{10} = S_0, H_{11} = S_1 - S_0,\ H_{12} = S_2 - S_1,\ H_{13} = S_3 - S_2, ...H_{1m} = S_m - S_{m-1}.$$

$$H_{10} + H_{11} + H_{12} + ... + H_{1m} = S_m = \sum_{j=0}^{m} H_{1j}(t)$$

Thus, we can write that

$$S_m(t) = \sum_{j=0}^{m} H_{1j}(t),\ E_m(t) = \sum_{j=0}^{m} H_{2j}(t),\ I_m(t) = \sum_{j=0}^{m} H_{3j}(t),$$

$$C_m(t) = \sum_{j=0}^{m} H_{4j}(t),\ R_m(t) = \sum_{j=0}^{m} H_{5j}(t),\ D_m(t) = \sum_{j=0}^{m} H_{6j}(t)$$

In the next theorem, we prove the existence of a solution.

Theorem 5.2
A solution to the fractional COVID-19 model (5) exists if there exists t_* such that

$$\frac{b_i t_*}{\Gamma(\eta)} < 1, \quad i = 1, 2, \ldots, 6.$$

Proof
From recursive technique, and equation (35), (36), we note that

$$\begin{aligned}\|H_{1m}(t)\| &\leq \frac{b_1}{\Gamma(\eta)}\int_0^t \|H_{1(m-1)}(\tau)\|d\tau \leq \left[\frac{b_1}{\Gamma(\eta)}\right]^2 \int_0^t\int_0^t \|H_{1(m-2)}(\tau)\|d\tau d\tau_1 \\ &\leq \ldots \leq \left[\frac{b_1}{\Gamma(\eta)}\right]^m \int_0^t\int_0^t \ldots \int_0^t \|H_{10}(\tau)\|d\tau d\tau_1 \ldots d\tau_m \\ &\leq \left[\frac{b_1}{\Gamma(\eta)}\right]^m \frac{t^m}{m!}\|S_m(0)\| \leq \left[\frac{b_1 t}{\Gamma(\eta)}\right]^m \|S_m(0)\|\end{aligned}$$

We obtain

$$\begin{aligned}\|H_{1m}(t)\| &\leq \left[\frac{b_1 t}{\Gamma(\eta)}\right]^m \|S_m(0)\| \\ \|H_{2m}(t)\| &\leq \left[\frac{b_2 t}{\Gamma(\eta)}\right]^m \|E_m(0)\| \\ \|H_{3m}(t)\| &\leq \left[\frac{b_3 t}{\Gamma(\eta)}\right]^m \|I_m(0)\| \\ \|H_{4m}(t)\| &\leq \left[\frac{b_4 t}{\Gamma(\eta)}\right]^m \|C_m(0)\| \\ \|H_{5m}(t)\| &\leq \left[\frac{b_5 t}{\Gamma(\eta)}\right]^m \|R_m(0)\| \\ \|H_{6m}(t)\| &\leq \left[\frac{b_6 t}{\Gamma(\eta)}\right]^m \|D_m(0)\|\end{aligned}$$

Thus, the system has a solution and also it is continuous. Now we show that the above functions construct solution for the model (5), we assume that

$$S(t) - S(0) = S_m(t) - A_{1m}(t)$$

Where

$$\begin{aligned}\|A_{1m}\| &= \|\frac{1}{\Gamma(\eta)}\int_0^t (t-\tau)^{\eta-1}\left(G_1(\tau, S(\tau)) - G_1(\tau, S_{m-1}(\tau))\right)d\tau\| \\ &\leq \frac{1}{\Gamma(\eta)}\int_0^t \|G_1(\tau, S(\tau)) - G_1(\tau, S_{m-1}(\tau))\|d\tau \\ &\leq \frac{b_1}{\Gamma(\eta)}\|S - S_{m-1}\|\, t\end{aligned}$$

Applying the above process recursively, we get

$$\|A_{1m}(t)\| \leq \left[\frac{b_1 t}{\Gamma(\eta)}\right]^{m+1} \cdot \frac{1}{(m+1)!}$$

At $m \longrightarrow \infty$, if $\left[\frac{b_1 t_*}{\Gamma(\eta)}\right] < 1$, then $\|A_{1m}\| \longrightarrow 0$, a same way

$$\begin{aligned}E(t) - E(0) &= E_m(t) - A_{2m}(t) \\ I(t) - I(0) &= I_m(t) - A_{3m}(t) \\ C(t) - C(0) &= C_m(t) - A_{4m}(t) \\ R(t) - R(0) &= R_m(t) - A_{5m}(t) \\ D(t) - D(0) &= D_m(t) - A_{6m}(t)\end{aligned}$$

Similarly, on using limit as $m \longrightarrow \infty$, if $\left[\frac{b_i t_*}{\Gamma(\eta)}\right] < 1,\ i = 2,3,4,5,6$ we obtain

$$\|A_{2m}\| \longrightarrow 0,\ \|A_{3m}\| \longrightarrow 0,\ \|A_{4m}\| \longrightarrow 0,\ \|A_{5m}\| \longrightarrow 0,\ \|A_{6m}\| \longrightarrow 0$$

□

Theorem 5.3
If the condition $(1 - \frac{b_i t}{\Gamma(\eta)}) > 0$ holds for $i = 1, 2, \ldots, 6$, then the system (5) has a unique solution.

Proof
To show the uniqueness of the solution, we suppose that the system has another solution such as $S_*(t), E_*(t), I_*(t), C_*(t), R_*(t), D_*(t)$ then we have

$$\begin{aligned} S(t) - S_*(t) &= \frac{1}{\Gamma(\eta)} \int_0^t (t-\tau)^{\eta-1} \left[G_1(\tau, S(\tau)) - G_1(\tau, S_*(\tau))\right] d\tau \\ \|S(t) - S_*(t)\| &\leq \frac{1}{\Gamma(\eta)} \int_0^t \|(t-\tau)^{\eta-1} \left[G_1(\tau, S(\tau)) - G_1(\tau, S_*(\tau))\right]\| d\tau \\ &\leq \frac{b_1}{\Gamma(\eta)} \|S(t) - S_*(t)\|\, t \end{aligned} \tag{37}$$

Thus

$$\|S(t) - S_*(t)\|(1 - \frac{b_1}{\Gamma(\eta)} t) \leq 0 \tag{38}$$

using hypothesis $(1 - \frac{b_1}{\Gamma(\eta)} t) > 0$, the last Eq (38) gets the form $\|S(t) - S_*(t)\| = 0$, It means that $S(t) = S_*(t)$. Applying the same procedure to each solution for $i = 2, 3, 4, 5, 6$ we obtain $E(t) = E_*(t), I(t) = I_*(t), C(t) = C_*(t), R(t) = R_*(t), D(t) = D_*(t)$. □

Remark 2: While the analytical condition requires $t < t^*$, this criterion is robustly satisfied in practice via the step-wise numerical progression of the simulation. Since all biological state variables of the COVID-19 system are strictly bounded within the compact feasible domain Φ, the localized uniqueness propagates sequentially, guaranteeing a unique and stable solution for the entire duration from 26 May 2020 to 20 March 2021.

6. Numerical Method and Data

6.1. Numerical scheme

To solve the system (5), we use the generalized Adams- Bashforth Moulton method [22]. To explain the method, consider the following nonlinear equation

$${}^C D_t^\eta y(t) = f(t, y(t)), y^{(k)}(0) = y_0^{(k)}, k = 0, 1, ..., n-1, \tag{39}$$

Where $\eta > 0$ and $n = [\eta]$ is the first integer not less than η . ${}^C D_t^\eta y(t)$ is the η-th order fractional derivative of $y(t)$ in the Caputo sense, which is defined in definition 2.1, by use of theorems 6.3 and 6.5, and f to be continuous and satisfy a Lipschitz condition, so the system (5) has one and only one solution defined on $[0, T]$. This solution solves the following Volterra integral equation:

$$y(t) = \sum_{k=0}^{n-1} y_0^{(k)} \frac{t^k}{k!} + \frac{1}{\Gamma(\eta)} \int_0^t (t-\tau)^{\eta-1} f(\tau, y(\tau)) d\tau, t \leq T. \tag{40}$$

Now numerical integration of differential equation (39) is transformed into numerical quadrature of an associated integral equation, (40). We used the Adams-Bashforth Moulton scheme for solving Eq (40), set

$tj = jh : j = 0, 1, ..., N$ with some integer N and step length $h = \frac{T}{N}$, and let $y_j \approx y(t_j)$. In detail, their derived computation scheme is as follows:

$$\begin{cases} y^p_{k+1}(t) = \sum_{j=0}^{n-1} \frac{t^j_{k+1}}{j!}\, y^{(k)}_0 + \frac{1}{\Gamma(\eta)} \sum_{j=0}^{k} b_{j,k+1}\, f(t_j, y(t_j)) \\ y_{k+1}(t) = \sum_{j=0}^{n-1} \frac{t^j_{k+1}}{j!}\, y^{(k)}_0 + \frac{1}{\Gamma(\eta)} \left(\sum_{j=0}^{k} a_{j,k+1}\, f(t_j, y(t_j)) + a_{k+1,k+1}\ f(t_{k+1}, y^p_{k+1}) \right) \end{cases} \tag{41}$$

Where

$$a_{j,k+1} = \frac{h^\eta}{\eta(\eta+1)} \begin{cases} k^{\eta+1} - (k-\eta)(k+1)^\eta & , \text{if } j = 0 \\ (k-j+2)^{\eta+1} + (k-j)^{\eta+1} - 2(k-j+1)^{\eta+1}, & \text{if } 1 \le j \le k \\ 1 & , \text{if } j = k+1 \end{cases} \tag{42}$$

and

$$b_{j,k+1} = \frac{h^\eta}{\eta} \left((k+1-j)^\eta - (k-j)^\eta \right),\ j = 0, 1, ..., k. \tag{43}$$

This computational scheme is very useful and efficient for numerical integration of fractional differential equations. In particular, it is successfully applied in computing chaotic attractors of fractional systems
Then we can write the system (5) as follows (41)

$$\begin{aligned} S_{k+1} &= \sum_{j=0}^{n-1} \frac{t^j_{k+1}}{j!}\, S^{(k)}_0 + \frac{1}{\Gamma(\eta)} \left(\sum_{j=0}^{k} a_{j,k+1}\, f(t_j, S_j) + a_{k+1,k+1}\ f(t_{k+1}, S^p_{k+1}) \right) \\ S_{k+1} &= S_0 + \frac{h^\eta}{\Gamma(\eta+2)} \left(-\frac{\gamma\, \beta(t)\, S^p_{k+1}\, I^p_{k+1}}{N} \right) + \frac{h^\eta}{\Gamma(\eta+2)} \sum_{j=0}^{k} a_{j,k+1} \left(-\frac{\gamma\, \beta(t)\, S_j\, I_j}{N} \right) \end{aligned}$$

As a similar way, we obtained

$$\begin{aligned} E_{k+1} &= E_0 + \frac{h^\eta}{\Gamma(\eta+2)} \left(\frac{\gamma\, \beta(t)\, S^p_{k+1}\, I^p_{k+1}}{N} - \sigma E^p_{k+1} \right) + \frac{h^\eta}{\Gamma(\eta+2)} \sum_{j=0}^{k} a_{j,k+1} \left(\frac{\gamma\, \beta(t)\, S_j\, I_j}{N} - \sigma E_j \right) \\ I_{k+1} &= I_0 + \frac{h^\eta}{\Gamma(\eta+2)} \left(\sigma E^p_{k+1} - \delta\, I^p_{k+1} \right) + \frac{h^\eta}{\Gamma(\eta+2)} \sum_{j=0}^{k} a_{j,k+1} \left(\sigma E_j - \delta\, I_j \right) \\ C_{k+1} &= C_0 + \frac{h^\eta}{\Gamma(\eta+2)} \left(\delta(1-\alpha) I^p_{k+1} - (\mu+\lambda) C^p_{k+1} \right) \\ &+ \frac{h^\eta}{\Gamma(\eta+2)} \sum_{j=0}^{k} a_{j,k+1} \left(\delta(1-\alpha) I_j - (\mu+\lambda) C_j \right) \\ R_{k+1} &= R_0 + \frac{h^\eta}{\Gamma(\eta+2)} \left(\delta I^p_{k+1} + \lambda C^p_{k+1} \right) + \frac{h^\eta}{\Gamma(\eta+2)} \sum_{j=0}^{k} a_{j,k+1} \left(\delta I_j + \lambda C_j \right) \\ D_{k+1} &= D_0 + \frac{h^\eta}{\Gamma(\eta+2)} \left(\mu C^p_{k+1} \right) + \frac{h^\eta}{\Gamma(\eta+2)} \sum_{j=0}^{k} a_{j,k+1} \left(\mu C_j \right) \end{aligned}$$

Where

$$
\begin{aligned}
S^p_{k+1} &= S_0 + \frac{1}{\Gamma(\eta)} \sum_{j=0}^{k} b_{j,k+1} \left(-\frac{\gamma\, \beta(t)\, S_j\, I_j}{N} \right) \\
E^p_{k+1} &= E_0 + \frac{1}{\Gamma(\eta)} \sum_{j=0}^{k} b_{j,k+1} \left(\frac{\gamma\, \beta(t)\, S_j\, I_j}{N} - \sigma\, E_j \right) \\
I^p_{k+1} &= I_0 + \frac{1}{\Gamma(\eta)} \sum_{j=0}^{k} b_{j,k+1} \left(\sigma E_j - \delta\, I_j \right) \\
C^p_{k+1} &= C_0 + \frac{1}{\Gamma(\eta)} \sum_{j=0}^{k} b_{j,k+1} \left(\delta(1-\alpha) I_j - (\mu+\lambda) C_j \right) \\
R^p_{k+1} &= R_0 + \frac{1}{\Gamma(\eta)} \sum_{j=0}^{k} b_{j,k+1} \left(\delta I_j + \lambda C_j \right) \\
D^p_{k+1} &= D_0 + \frac{1}{\Gamma(\eta)} \sum_{j=0}^{k} b_{j,k+1} \left(\mu C_j \right)
\end{aligned}
$$

6.2. Data sources and study period

The COVID-19 data were collected from public and official sources, including the National Institute for Communicable Diseases (NICD), the South African Department of Health, the COVID-19 South Africa data repository, the COVID-19 South Africa Dashboard, World Health Organization data, and publicly available epidemiological reports [26, 27, 28, 1]. The dataset includes confirmed cases, deaths, recoveries, and ICU cases. Daily reported incidence was computed from cumulative confirmed cases using first differences. The study period is from 26 May 2020 to 20 March 2021, corresponding to the interval over which both incidence and ICU cases data were consistently available. The initial active human population was set at $N(0) = 59{,}308{,}690$, based on Statistics South Africa mid-2020 estimates [29], serving as the upper bound for the active population dynamics over the studied timeframe.

6.3. Parameter estimation methodology

The numerical optimization and parameter estimation pipeline was configured to ensure full reproducibility, addressing all calibration settings and constraints essential for the fractional-order SEICRD model. The implementation process is detailed as follows:

- **Objective Function:** A non-linear Least Squares cost function was minimized to reduce the discrepancy between the model outputs and empirical data. The algorithm minimized a flattened vector of residuals representing the differences between the observed daily cases, ICU occupancy, and recovered counts and their model-predicted counterparts.
- **Numerical Integration:** The system of fractional-order differential equations was solved numerically at each step using the Adams-Bashforth-Moulton (ABM) predictor-corrector method. To ensure temporal consistency, model outputs were aligned with empirical time series via linear interpolation, and cumulative recovered counts were converted into daily increments using the first-order difference operator (`np.diff`).
- **Computational Robustness:** To maintain numerical stability, an exception-handling mechanism was integrated into the objective function to manage non-finite values (NaN) during the optimization process, effectively returning a penalty vector to prevent solver failure.
- **Convergence Tolerance:** The optimization routine terminated based on the default convergence criteria for function and variable tolerances (typically 1×10^{-8}), ensuring high-fidelity parameter convergence.

- **Optimizer and Constraints:** Parameters were estimated via the Python `scipy.optimize.least_squares` routine, utilizing the Trust Region Reflective (TRF) algorithm. To ensure biological plausibility, explicit lower and upper `bounds` were imposed on the parameter space, restricting estimates to physically meaningful ranges.
- **Software Version:** All mathematical simulations, trajectory tracking, and statistical fits were performed using Python 3.10 with the `scipy` (v1.15), `numpy`, and `pandas` libraries.

7. Results and Discussion

7.1. Estimated parameters and epidemiological interpretation

The parameters of the fractional-order model were estimated using daily cases, daily recovered cases and the cases in intensive care of COVID-19 over the period from 26 May 2020 to 20 March 2021, which corresponds to the first and second epidemic waves in South Africa. All parameters of the model, including the fractional-order parameter, were estimated and are reported in Table 2 together with the search bounds. For the epidemiological rates and the fractional order we additionally report 95% asymptotic confidence intervals, computed from the covariance matrix $\hat{\sigma}^2\,(J^\top J)^{-1}$, in which J is the Jacobian of the least-squares residuals evaluated at the estimate and $\hat{\sigma}^2$ is the residual variance; these intervals are conditional on the fitted intervention timeline $\beta(t)$ and, being based on the local curvature at the estimate, should be read together with the profile analysis of the fractional order in Section 7.4, which indicates that η itself is only weakly identified. As detailed in the note to Table 2, the rates λ and μ are not separately identifiable from the infected, ICU, and recovered series and are therefore summarised through the identifiable combination $\mu + \lambda$. The resulting values describe the epidemic dynamics over the study period.

In Figures 2, 3, and 4, the daily COVID-19 cases are represented by points, while the model fitted to this data is shown as a solid line. These figures illustrate how the model captures both daily, ICU, and daily recovered COVID-19 cases during the first and second waves in South Africa. Similarly, Figures 5 and 6 depict the estimated infectious communication rate $\beta(t)$ and the effective reproduction number $\mathcal{R}_{eff}$ for these waves. To represent the time-dependent nature of these dynamics, we employ the Woods–Saxon potential function, which acts as a flexible mathematical framework to model the continuous shifts in transmission rates resulting from evolving public health interventions. The vertical lines in these figures denote critical policy shifts, marking the timing of different lockdown levels—from Level 3 down to Level 1 and subsequent adjustments. These lines illustrate how abrupt or gradual changes in non-pharmaceutical interventions (NPIs) correlate with the observed fluctuations in $\beta(t)$ and $\mathcal{R}_{eff}$, providing visual evidence of the direct impact of government policies on the epidemic trajectory. The estimated parameter values are then used to calculate $\mathcal{R}_{eff}$, $\beta(t)$, and $\mathcal{R}_0$, as well as to perform forecasts for current measurements and other potential scenarios.

The effective contact rate $\gamma = 0.083872$ represents the intensity of disease transmission between susceptible and infectious individuals. Its estimated value indicates a moderate transmission level, reflecting the impact of non-pharmaceutical interventions. The transition rate from exposed to infectious individuals, $\sigma = 0.234465$, corresponds to an average incubation period of approximately $1/\sigma \approx 4.26$ days [23].

The estimated parameter $\delta = 0.482507$ reflects the rapid turnover of reported active cases within the surveillance registry. This value should be interpreted as the effective removal rate—encompassing both recovery and transition to critical illness—rather than the natural recovery rate of total infections. This high rate is attributed to the aggressive public health interventions and prompt isolation protocols implemented during the study period. Furthermore, the inclusion of daily recovered data in our model increases the outflow from the infectious class, which inherently contributes to the elevated value of δ. This interpretation is consistent with the clinical profile of the epidemic surges in South Africa and is supported by the data in Table 2; specifically, the low transition rate to critical care ($\lambda = 0.0313$) indicates that the majority of cases did not progress to the ICU stage, thereby maintaining a rapid turnover of reported active cases. The parameter $\alpha = 0.984075$ represents the proportion of infectious individuals who do not require admission to the intensive care unit. Its high value indicates that the majority of infections were mild or moderate, with only a small fraction (approximately 1.6%) progressing to

Table 2. Estimated parameters, initial conditions, and search bounds

Symbol	Estimated Value	95% CI	Bounds	Reference
Estimated Parameters				
γ	0.083872	[0.0667, 0.1010]	[0.001, 1]	Fitted
σ	0.234465	[0.2051, 0.2638]	[0.001, 1]	Fitted
δ	0.482507	[0.3871, 0.5779]	[0.001, 1]	Fitted
α	0.984075	[0.9710, 0.9972]	[0.01, 1]	Fitted
λ	0.031396	†	[0.001, 1]	Fitted
μ	0.012063	†	[0.0001, 0.1]	Fitted
a_0	1	–	-	Assumed
z_1	-17.326286	–	[-100, 100]	Fitted
t_{tu}	135.946054	–	[1, 200]	Fitted
b_{Duration_1}	12.503783	–	[0.1, 50]	Fitted
z_2	28.952336	–	[-100, 100]	Fitted
t_{tu1}	127.024781	–	[1, 300]	Fitted
b_{Duration_2}	59.994385	–	[1, 60]	Fitted
η	0.975000	[0.9653, 0.9847]	[0.5, 1]	Fitted
Initial Conditions ($t = 0$)				
$S(0)$	59,308,690	–	-	computed
$E(0)$	293.836359	–	[1, 100000]	Fitted
$I(0)$	1,673	–	-	Data
$C(0)$	195	–	-	Data
$R(0)$	710	–	-	Data
$D(0)$	28	–	-	Data
$N(0)$	59,308,690	–	-	Statistics South Africa mid-2020 estimates

† The recovery rate λ and the ICU mortality rate μ are not separately identifiable from the observed infected, ICU, and recovered series (their estimates are almost perfectly anti-correlated, since they enter the observable dynamics only through the ICU-exit combination $\mu + \lambda$); only the combined ICU-exit rate $\mu + \lambda = 0.0435$, with 95% confidence interval $[0.0034, 0.0835]$, is identified. All reported confidence intervals are conditional on the fitted transmission timeline $\beta(t)$.

critical illness[28]. This interpretation is validated by clinical data from the study period, which confirms that the vast majority of infected individuals recovered without requiring ICU admission. This is consistent with local hospitalization records, showing that only a small proportion of confirmed cases required critical care, thereby justifying the high estimated value of α within our compartmental model and demonstrating that the epidemic burden was primarily driven by non-critical cases managed outside the intensive care units.

The parameter $\lambda = 0.031396$ corresponds to an average ICU stay of approximately 32 days, whereas the mortality rate $\mu = 0.012063$ represents deaths occurring in the critical class and remains relatively low during the study period. The fractional order $\eta = 0.975$ indicates the presence of weak but non-negligible memory effects in the epidemic dynamics. This implies that the current spread of the disease is mildly influenced by past infection levels and previous interventions, while the system remains close to the behavior of a classical integer-order model [24, 25].

To describe changes in transmission intensity over time, the infectious communication rate was modeled using a Woods-Saxon type function. The parameters z_1 and b represent the timing and smoothness of the transition during the first epidemic wave. The value $z_1 = -17.326286$ shows that the reduction in contact intensity started before the observation period, reflecting the early implementation of control measures. This pattern aligns with the epidemiological situation in South Africa, where, from May 1, 2020, a level 4 lockdown was implemented. These restrictions were gradually eased to levels 3, 2, and 1. The parameter $b_{\text{Duration}_1} = 12.503783$ controls the smoothness of this transition, indicating a gradual decline in transmission. The timing parameter $t_{tu} = 135.946054$ marks the main transition point of the first wave.

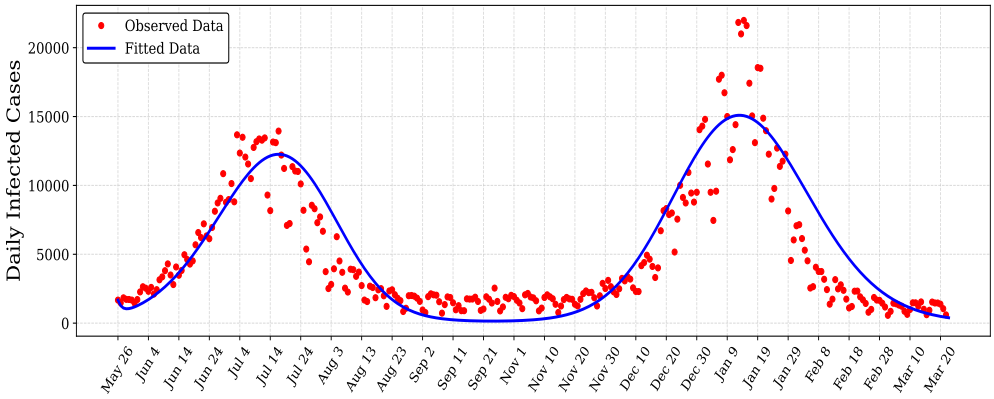

Figure 2. Model fit of the daily cases of COVID-19 in the first and second wave between 26 May 2020 to 20 March 2021.

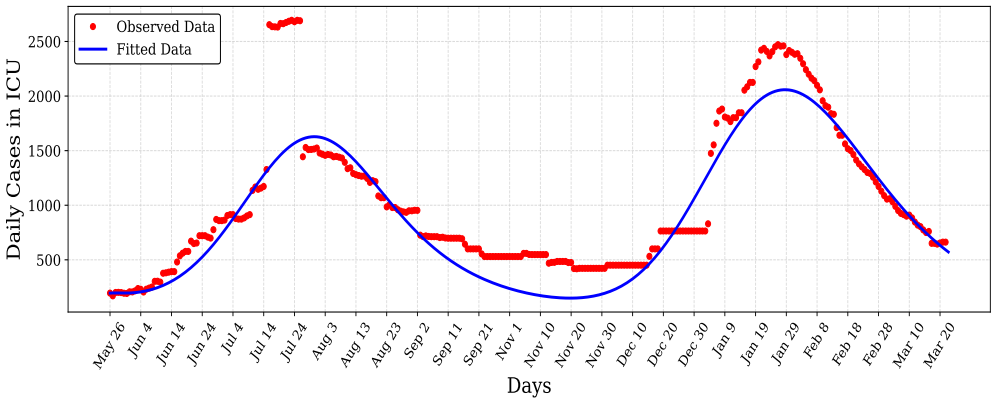

Figure 3. Model fit of the daily cases of COVID-19 in the Intensive Care Unit in the first and second wave between 26 May 2020 to 20 March 2021.

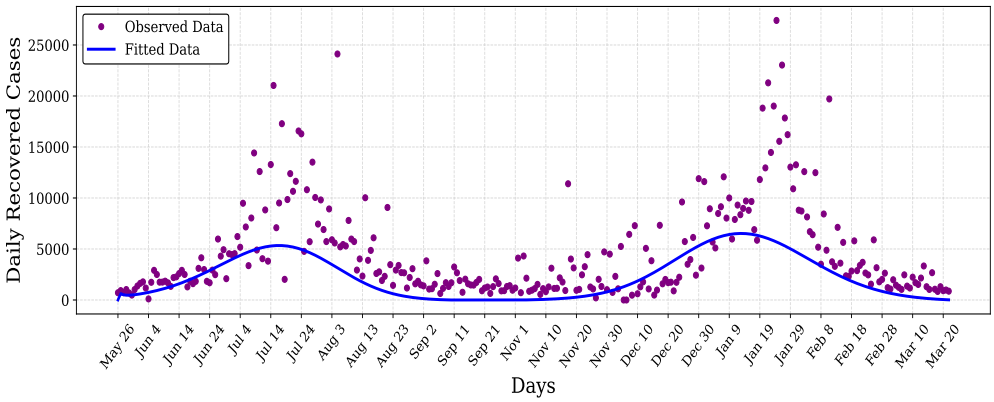

Figure 4. Model fit of the daily recovered cases of COVID-19 in the first and second wave between 26 May 2020 to 20 March 2021.

For the second wave, the parameters $z_2 = 28.952336$ and $b_{\text{Duration}_2} = 59.994385$ describe a renewed increase in transmission intensity. The positive value of z_2 shows that this increase happened within the observation period. The relatively large value of b_{Duration_2} indicates that the transition was more gradual and prolonged than in the first

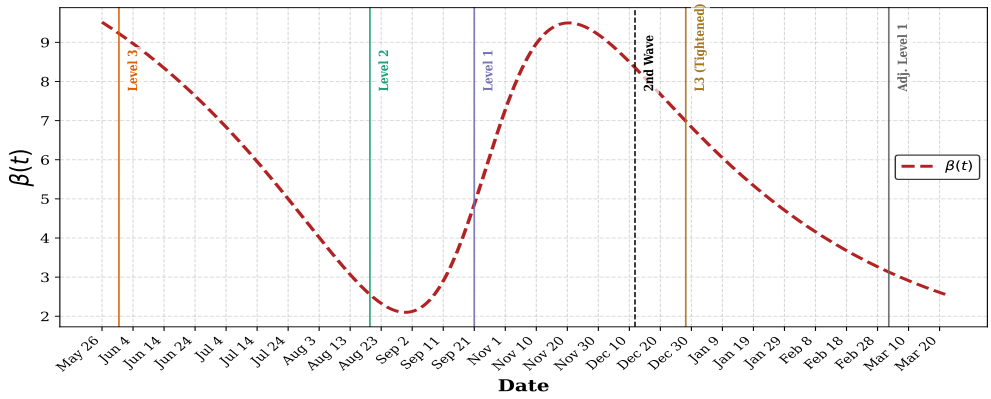

Figure 5. Infectious communication rate (Hazard rate of infection)

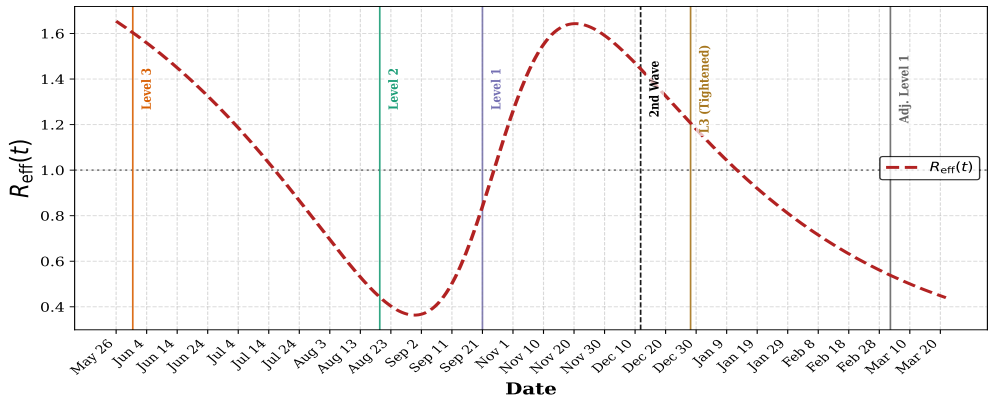

Figure 6. Effective reproduction number $\mathcal{R}_{eff}$

wave. The timing parameter $t_{tu1} = 127.024781$ indicates the start of this second wave. The proximity of t_{tu} and t_{tu1} shows that the first and second waves overlap in time. Although this proximity may raise questions regarding the structural identifiability of the Woods-Saxon parameters, it accurately reflects the epidemiological reality in South Africa, where the second wave emerged before the first had fully subsided. Mathematically, the Woods-Saxon function effectively captures distinct changes in the slope of the transmission rate, rather than relying solely on a single turning point. Given the significant differences in the intensity and shape of the second wave compared to the first, the estimation algorithm distinguished the two phases well enough to reproduce both waves in the fitted $\beta(t)$; as discussed in Section 8, however, the individual Woods-Saxon parameters remain correlated, and the confidence intervals reported for the epidemiological rates are accordingly conditional on this fitted transmission timeline. Mathematically, this construction allows the infectious communication rate to change continuously without sudden jumps. Epidemiologically, it reflects a realistic situation in which the easing of interventions and behavioral changes led to renewed transmission while residual infections from the first wave were still present.

7.2. Sensitivity analysis

To thoroughly evaluate the dynamics of the epidemic model, we performed two complementary types of sensitivity analysis: first, an analytical sensitivity analysis on the basic reproduction number ($\mathcal{R}_0$); and second, a numerical local sensitivity analysis on the peak epidemic metrics across separate waves.

Definition 7.1
The sensitivity index of $\mathcal{R}_0$ with respect to a parameter P is given by

$$C_P^{\mathcal{R}_0} = \frac{\partial \mathcal{R}_0}{\partial P} \times \frac{P}{\mathcal{R}_0}$$

Then, we have

$$\begin{aligned}
\frac{\partial \mathcal{R}_0}{\partial \beta_0} &= \frac{\gamma}{\delta} \times \frac{\beta_0}{\frac{\gamma\,\beta_0}{\delta}} = 1 \\
\frac{\partial \mathcal{R}_0}{\partial \delta} &= \frac{-\gamma\,\beta_0}{\delta^2} \times \frac{\delta}{\frac{\gamma\,\beta_0}{\delta}} = -1 \\
\frac{\partial \mathcal{R}_0}{\partial \gamma} &= \frac{\beta_0}{\delta} \times \frac{\gamma}{\frac{\gamma\,\beta_0}{\delta}} = 1
\end{aligned}$$

The sensitivity indices $\beta_0 = +1, \gamma = +1$ mean that any change in β_0 or γ will have a direct and proportional effect on $\mathcal{R}_0$ (an increase or decrease in the same direction). In a similar fashion, the sensitivity index $\delta = -1$ means that any change in δ will have a reverse and proportional effect on $\mathcal{R}_0$.

To extend our evaluation beyond $\mathcal{R}_0$ and understand how different parameters affect the multi-wave epidemic structure, we performed a numerical local sensitivity analysis using a 5% change in parameter values. We analyzed the first and second waves separately to see how peak infections (I_{peak}), peak timing (t_{peak}), and peak ICU demand (C_{peak}) are influenced. The results show clear and logical differences between the two waves:

- **Effective Transmission Rate (γ):** This parameter has a strong positive effect on both waves. Its impact is much larger in the second wave (the sensitivity index increases from 13.65 to 69.08), which shows that controlling transmission becomes increasingly vital as the epidemic progresses.
- **Recovery Rate without ICU (α):** This represents the rate of recovery without being in ICU. It has a strong negative impact on ICU demand ($C_{peak1} = -17.60$, $C_{peak2} = -22.98$). This mathematically proves that improving early medical care directly reduces hospital overcrowding.
- **Wave Characteristics ($z_2, t_{\text{Duration}_2}$):** The parameters controlling the second wave have a dominant effect on the global peak (with sensitivities exceeding 250), confirming their key role in shaping the multi-wave structure of the outbreak.

7.3. Scenario simulations

In this section, numerical simulations and epidemiological analysis are performed using South African COVID-19 data. Several scenarios are considered by varying the model parameters. According to Table 2, the effective transmission rate is estimated at $\gamma = 0.0838$. Figure 7 demonstrates the high sensitivity of both daily infected cases and ICU admissions to variations in γ. At the baseline value of $\gamma = 0.0838$, the model predicts two distinct waves, with peaks of approximately 12,260 and 15,090 for infected cases, and 1,627 and 2,057 for ICU admissions. Reducing γ to 0.083 significantly mitigates these peaks, whereas increasing it to 0.085 results in a substantial surge, with peaks reaching approximately 14,088 and 22,851 (infected) and 1,862 and 3,108 (ICU).

These parameter variations are directly linked to public health outcomes; for instance, a reduction in γ from 0.084 to 0.083 can be interpreted as the impact of implementing non-pharmaceutical interventions (NPIs), such as an earlier lockdown or stricter social distancing protocols. Conversely, an increase in γ reflects the relaxation of such measures. These findings underscore the critical impact of intervention timing on disease dynamics and validate the potential efficacy of adaptive public health strategies.

From Table 2, the recovery rate of ICU patients during the COVID-19 pandemic is estimated as $\lambda = 0.0313$. Figure 9 illustrates the effect of changing the recovery rate λ of ICU patients on the dynamics of the ICU population during the first and second waves. Figure 9 illustrates the effect of varying λ on the ICU population during the two waves. At the estimated value $\lambda = 0.0313$, peaks occur around 1 August 2020 with approximately $1,627$

Table 3. Normalized sensitivity indices of the SEICRD model parameters on the peak infection size (I_{peak}), peak timing (t_{peak}), and peak ICU demand (C_{peak}) for the first and second epidemic waves, evaluated using a 5% perturbation.

Parameter	Wave 1			Wave 2		
	I_{peak1}	t_{peak1}	C_{peak1}	I_{peak2}	t_{peak2}	C_{peak2}
γ	13.6525	1.0345	13.1391	69.0788	0.2679	68.1923
σ	2.4542	0.0000	2.3117	3.4328	0.0000	3.3026
δ	-7.5213	-1.0345	-6.7065	-15.7950	-0.2679	-15.5335
α	-0.0008	0.0000	-17.6043	-0.0256	0.0000	-22.9818
λ	0.0000	0.0000	-0.4751	-0.0003	0.0000	-0.4936
μ	0.0000	0.0000	-0.1848	0.0003	0.0000	-0.1923
z_1	-13.0384	-3.4483	-12.7899	-20.0041	6.6964	-19.5737
t_{Duration_1}	-0.0771	0.0000	-0.1052	-17.6010	0.0893	-17.5072
b_1	0.0761	0.0000	0.0949	0.0022	0.0000	0.0322
z_2	87.4566	3.7931	84.4525	426.4839	-0.6250	408.2358
t_{Duration_2}	15.3732	2.0690	15.3230	267.0529	0.0893	259.3558
b_2	-6.5433	-1.3793	-6.3865	-4.6235	0.5357	-4.5440

ICU patients in the first wave, and at the end of January 2021 with around $2,057$ patients in the second wave. Decreasing λ to 0.02 significantly increases these peaks to $1,972$ and $2,527$, respectively. Conversely, increasing λ to 0.04 mitigates the burden on the healthcare system, reducing peaks to approximately $1,435$ and $1,806$. These results highlight that enhancing clinical recovery protocols is as crucial as reducing transmission for managing ICU capacity.

Figure 10 illustrates the effect of varying the parameter α on the peak size of the ICU patient population during the first and second waves. For the estimated value $\alpha = 0.98$, the peak occurs on the 1st of August 2020 with approximately $2,041$ ICU patients during the first wave, and at the end of January with around $2,584$ ICU patients during the second wave. When the value of α is decreased to 0.97, the peak size of the ICU patient population increases to about $3,055$ patients in the first wave and $3,877$ patients in the second wave. In contrast, increasing α to 0.99 leads to a reduction in the peak size, which decreases to approximately $1,027$ ICU patients in the first wave and $1,292$ ICU patients in the second wave.

These findings have critical implications for healthcare capacity management. Our simulations demonstrate that interventions aimed at increasing λ or α, or decreasing γ, are essential to keep ICU demand below maximum bed capacity. By maintaining demand within these operational thresholds, such interventions effectively prevent system collapse and ensure the continuity of quality care during epidemic surges.

Figures 11 and 12 show the effect of varying β_0 on the peak sizes of the infected and ICU populations during two epidemic waves, with changes in β_0 driven by the parameter Z_1. For $\beta_0 = 9.515$, the infected population peaks at approximately $12,260$ in the first wave and $15,090$ in the second wave, while the ICU population peaks at about $1,627$ and $2,057$, respectively. Reducing β_0 to 8.842 lowers the peaks to around $5,313$ and 930 for the infected population and to approximately 723 and 130 for ICU patients. Conversely, increasing β_0 to 9.842 raises the peaks to about $19,040$ and $37,590$ for infected individuals and to $4,716$ and $9,621$ for ICU patients during the two waves.

Figures 13 and 14 illustrate the effect of varying β_0 driven by the parameter Z_2. For $\beta_0 = 9.515$, the infected population peaks at roughly $12,260$ and $15,090$ in the first and second waves, respectively, while the ICU population peaks at about $1,627$ and $2,057$. Decreasing β_0 to 8.6 reduces the infected population peaks to around $4,568$ and 362 and lowers ICU peaks to $1,167$ and 99. In contrast, increasing β_0 to 10.45 increases the infected peaks to approximately $40,824$ and $174,565$ and raises ICU peaks to $5,303$ and $23,301$ during the two waves.

7.4. Fractional versus integer-order model selection

To rigorously evaluate the statistical justification of the fractional-order framework, a comprehensive quantitative comparison between the fractional model ($\eta = 0.975$) and the classical integer-order model ($\eta = 1.0$) was

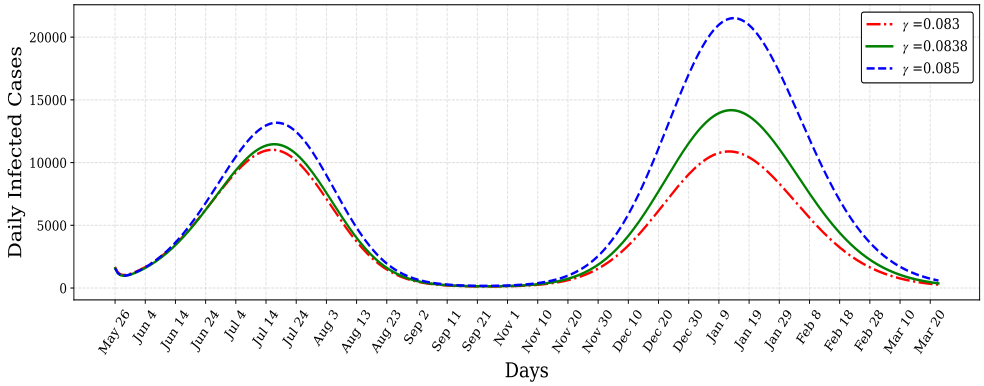

Figure 7. The evolution of infected population with different value of the Effective transmission rate γ.

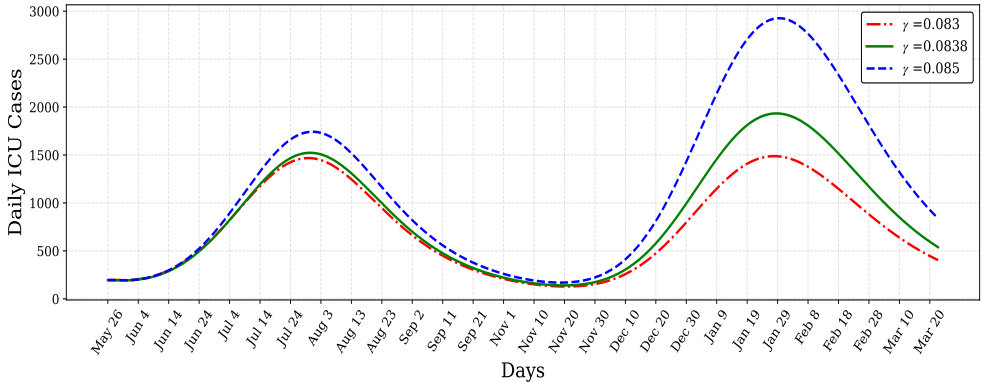

Figure 8. The evolution of infected population with different value of the Effective transmission rate γ.

conducted using Root Mean Square Error (RMSE), Mean Absolute Error (MAE), the coefficient of determination (R^2), and the Akaike Information Criterion (AIC), as summarized in Table 4. The results demonstrate that the fractional-order framework achieves substantial improvements across key epidemiological compartments. Specifically, for active infections and intensive care unit (ICU) cases, the fractional model exhibits dramatic reductions in error metrics. For instance, the RMSE for infections drops significantly from 4479.20 in the integer-order model to 2253.40 in the fractional model, while the MAE decreases from 2906.49 to 1653.57. A similar improvement is observed in ICU cases, where the RMSE decreases from 573.09 to 306.48. Although the integer-order model yields a slightly lower error in the recovered compartment, the overall aggregate performance favors the fractional approach for this parameterisation. The comparatively modest recovered-compartment fit stems from how recoveries were reported rather than from the dynamics: in the South African feed, recoveries were reconstructed administratively and are recorded incompletely and inconsistently relative to confirmed cases. We therefore relate the observed and modelled recoveries through $R^{\mathrm{obs}}(t) = \rho\, R(t)$ and estimate the recovered-reporting factor ρ conditionally on the fitted dynamics, obtaining $\rho = 1.84$ (95% CI $[1.71, 1.96]$). Because ρ scales only the recovered read-out and R is a terminal compartment, the state trajectories, the infected and ICU fits, and all epidemiological estimates in Table 2 are left unchanged; after the adjustment the recovered fit improves substantially (daily R^2 rising from 0.165 to 0.465, with a cumulative-recovered correlation of 0.99), confirming that the low raw R^2 reflected a reporting-scale mismatch rather than a deficiency of the model dynamics. The overall RMSE decreases from 3274.81 to 2395.42, and the overall MAE drops from 1862.86 to 1404.45. Furthermore,

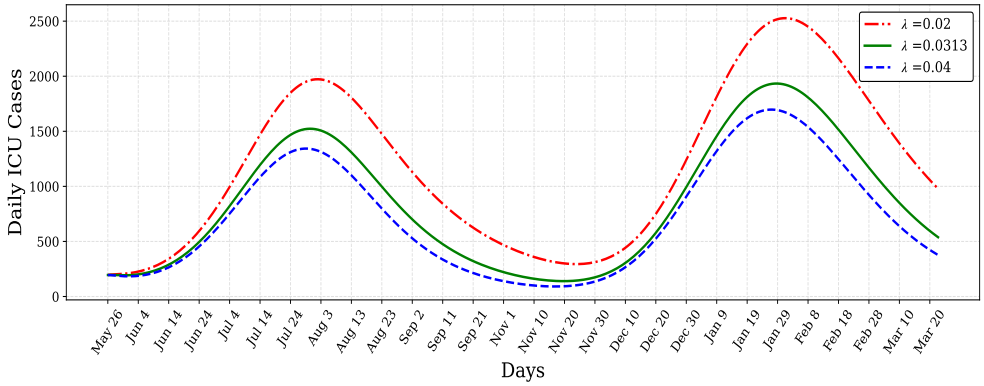

Figure 9. The evolution of infected population in ICU with different value of the Recovery rate of ICU patient λ.

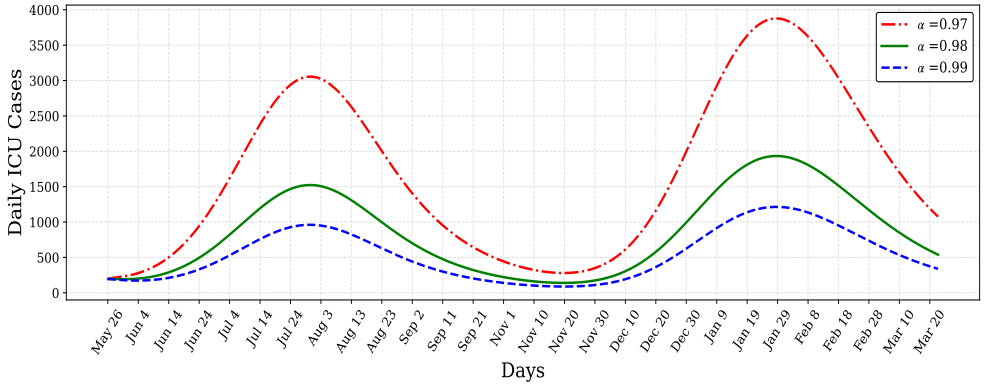

Figure 10. The evolution of infected population in ICU with different value of the Recovery rate without being in ICU α.

the Akaike Information Criterion (AIC) decreases from 14597.23 for the integer-order model to 14036.36 for the fractional model, yielding a substantial ΔAIC of 560.87. While a ΔAIC of this magnitude would ordinarily be read as strong support for the fractional model, the estimated order lies close to unity, so we assessed how sharply η is determined by the data through a profile analysis: the order was fixed on a grid over $[0.90,\ 1.0]$ and the remaining parameters were re-optimised at each value. As shown in Figure 15, the shape of this profile depends on how the remaining parameters are constrained. When they are held within biologically plausible ranges, the minimised error decreases weakly and monotonically toward the integer order $\eta = 1$; when they are left unconstrained, a shallow minimum appears near $\eta = 0.975$, but only because the optimiser then drives the epidemiological rates to non-physical values (sub-day incubation and illness durations) and the unobserved mortality rate μ toward zero. In either case the variation is modest, and the ordering of the fractional and integer fits is not robust to these choices, so the data do not decisively single out a non-integer order. We therefore interpret the comparison conservatively: the fractional formulation ($\eta = 0.975$) fits the observed infected and ICU compartments at least as well as the integer-order model while providing a parsimonious mechanistic account of memory effects, but we do not claim that the data decisively single out a non-integer order. This weak identifiability of η, together with the correlations among the remaining parameters, is discussed in Section 8.

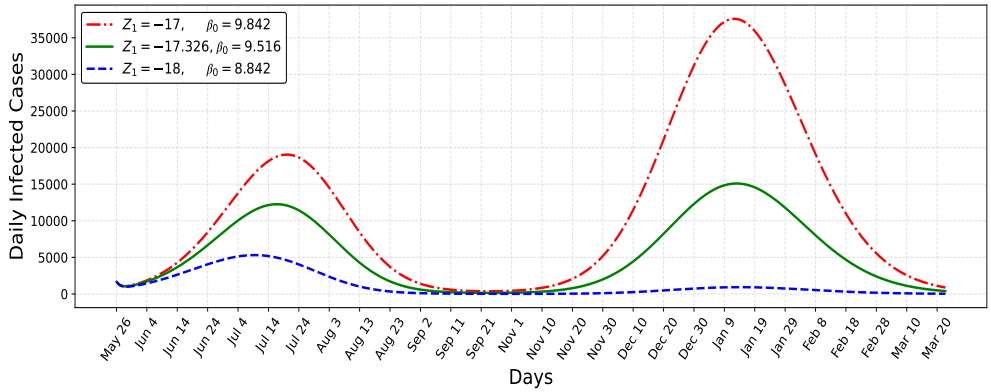

Figure 11. The evolution of infected population with different value of Z_1 and value $\beta(t)$ and β_0 corresponding to Z_1.

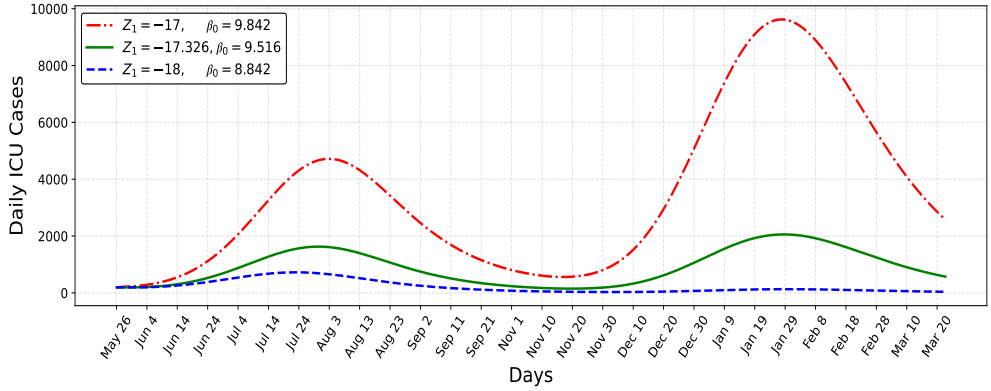

Figure 12. The evolution of infected population with different value of Z_1 and value $\beta(t)$ and β_0 corresponding to Z_1.

Table 4. Goodness-of-Fit Test Statistics and Model Selection Metrics Comparing Fractional-Order ($\eta = 0.975$) and Classical Integer-Order ($\eta = 1.0$) Formulations. The recovered compartment is evaluated after a constant recovered-reporting factor ρ ($\rho = 1.84$ for the fractional and 1.11 for the integer fit; see text); without this adjustment the recovered R^2 is 0.165 and 0.462, respectively. The recovered and overall rows incorporate this factor; the infected and ICU rows are unaffected.

Output Class	**Order (η)**	**RMSE**	**MAE**	R^2	**AIC**
Infected (I)	0.975	2253.40	1653.57	**0.7750**	4660.12
	1.000	4479.20	2906.49	0.1112	5070.32
ICU (C)	0.975	306.48	200.30	**0.7924**	3463.10
	1.000	573.09	415.89	0.2740	3836.63
Recovered (R)	0.975	3470.21	2359.48	0.4652	4921.18
	1.000	3432.42	2266.20	**0.4768**	**4912.61**
Overall System	0.975	**2395.42**	**1404.45**	**0.6889**	**14036.36**
	1.000	3274.81	1862.86	0.4186	14597.23

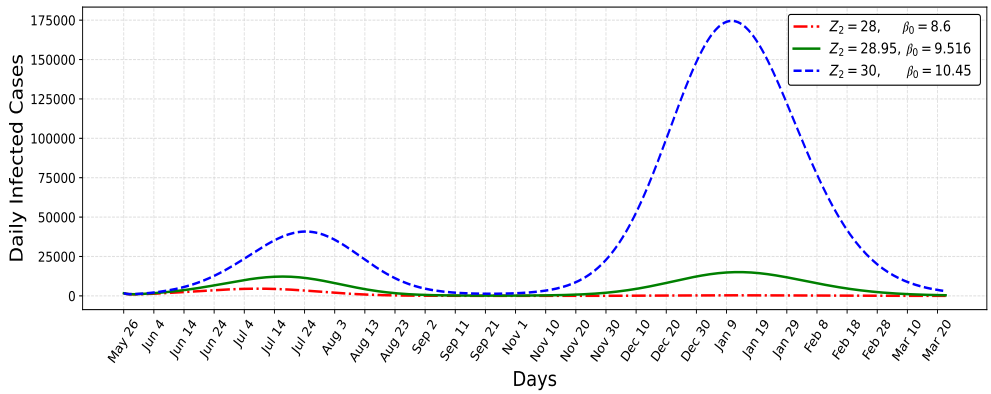

Figure 13. The evolution of infected population with different value of Z_2 and value $\beta(t)$ and β_0 corresponding to Z_2.

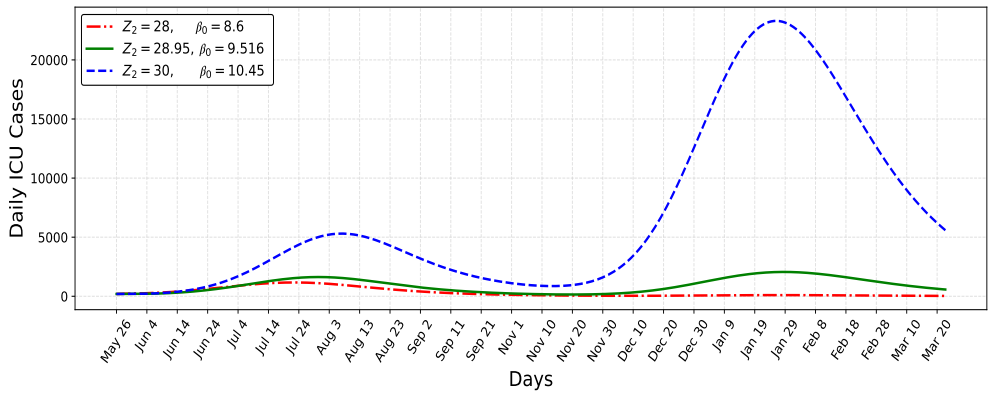

Figure 14. The evolution of infected population with different value of Z_2 and value $\beta(t)$ and β_0 corresponding to Z_2.

7.5. Model validation

Beyond the aggregate error metrics of Table 4, we assess the adequacy of the fitted models through residual diagnostics and an out-of-sample hold-out experiment.

Figure 19 shows the residuals (model $-$ data) for the infected, ICU, and recovered compartments, together with their empirical distributions, for both the fractional ($\eta = 0.975$) and integer-order ($\eta = 1.0$) fits. The integer-order model exhibits a pronounced systematic bias in the infected compartment (mean residual $\approx 2.5 \times 10^3$), consistent with its tendency to overshoot the epidemic peaks, whereas the fractional model reduces this mean residual by roughly an order of magnitude and yields residual distributions that are more tightly centred about zero. As is typical for daily epidemic time series, both models retain positive serial correlation in the residuals (Durbin–Watson statistics well below 2); the fractional model attenuates this correlation for the infected and ICU compartments, indicating a better-specified temporal structure.

In the top row of Figure 19 are the residuals versus time for the infected (I), ICU (C), and recovered (R) compartments. In the bottom row are the corresponding residual distributions.

To probe generalisability beyond the calibration sample, we performed a random $80/20$ hold-out: the model was re-estimated on a random 80% of the daily observations and evaluated on the remaining 20% (60 held-out days distributed across both waves). This produced an out-of-sample $\mathrm{RMSE} = 2115$ and $\mathrm{MAE} = 1161$ across the active compartments, comparable to the in-sample errors of Table 4 and indicating that the fit is not an artefact

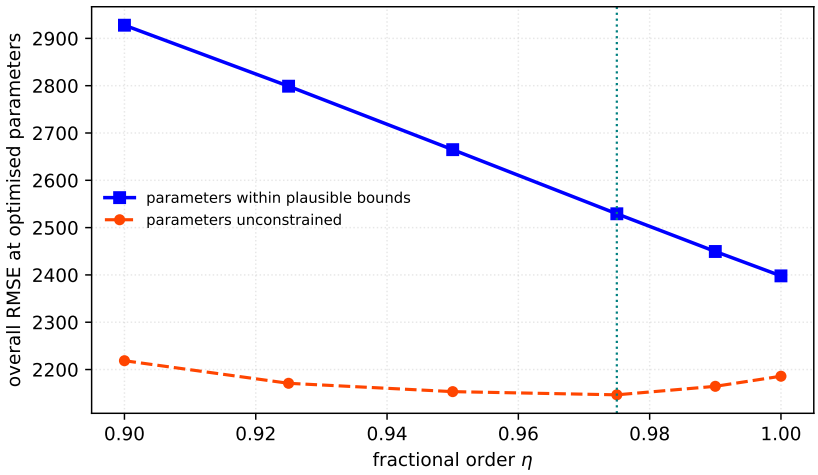

Figure 15. Profile of fit quality over the fractional order η. For each fixed η the remaining parameters were re-optimised against the observed infected, ICU, and recovered series. Within biologically plausible parameter bounds (squares) the minimised RMSE decreases weakly toward the integer order $\eta = 1$; with the parameters unconstrained (circles) a shallow minimum appears near $\eta = 0.975$, attained only at non-physical parameter values. The fractional order is therefore weakly identified, and the fractional-versus-integer ordering is sensitive to the constraints imposed.

of over-parameterisation. We stress that this is an interpolative assessment. When the split is instead temporal—training on the first 80% of the window and predicting the unseen final 20%—the error rises substantially (RMSE $\approx 6.3 \times 10^3$), reflecting the intrinsic difficulty of anticipating a second wave whose intervention timeline is absent from the training period. The out-of-sample results should accordingly be read as evidence against in-sample overfitting rather than as a claim of forward-forecasting skill.

7.6. Public-health implications

The scenario analysis translates directly into operational guidance for epidemic preparedness. Integrating the ICU trajectories over the study period, the fractional model attributes $274{,}733$ cumulative ICU patient-days to the two waves, compared with $400{,}575$ patient-days projected by the integer-order model; the memory-driven attenuation therefore corresponds to about $125{,}842$ ICU bed-days, a difference of direct relevance to hospital capacity planning in a resource-constrained setting. Because the reductions achievable through the transmission rate γ and the non-ICU recovery fraction α are strongly nonlinear, the timing of intervention is as consequential as its magnitude: in our simulations, initiating contact-reduction measures 7–10 days ahead of a turning point t_{Turning} produced a disproportionate reduction in peak ICU overflow. These findings support a preparedness strategy that balances the socio-economic cost of restrictions against health-system preservation, favouring early, temporary tightening of non-pharmaceutical interventions over later, more prolonged measures.

8. Limitations

Several structural assumptions bound the scope of the present analysis and should be borne in mind when interpreting the results.

- **Homogeneous mixing and demographics.** The model assumes a well-mixed population and omits age-stratified contact structure and spatial movement between provinces, both of which shaped transmission heterogeneity in South Africa.

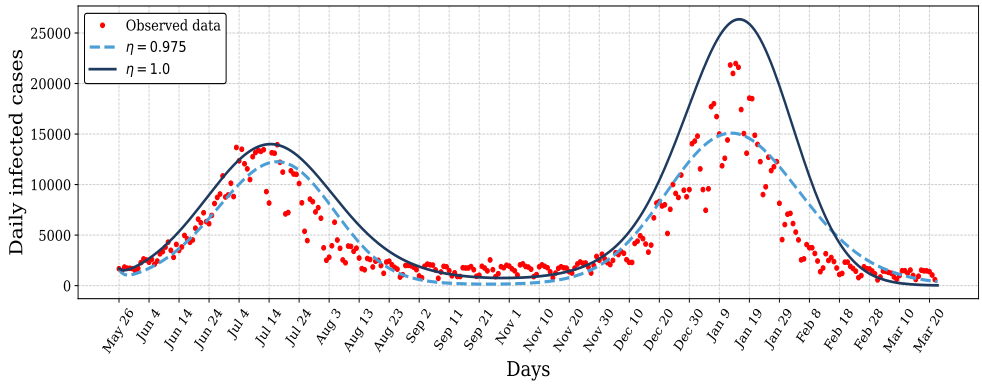

Figure 16. Model fit of the daily cases of COVID-19 cases for different fractional derivative orders η, with parameters estimated for each value of η.

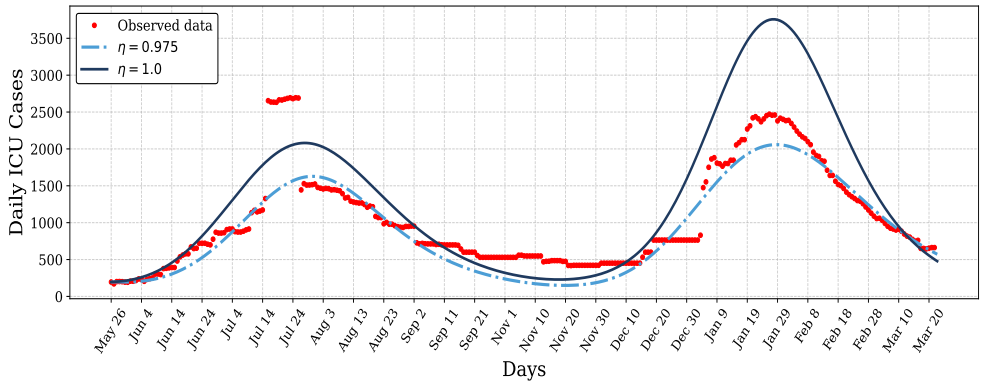

Figure 17. Model fit of the daily cases of COVID-19 in the Intensive Care Unit for different fractional derivative orders η, with parameters estimated for each value of η.

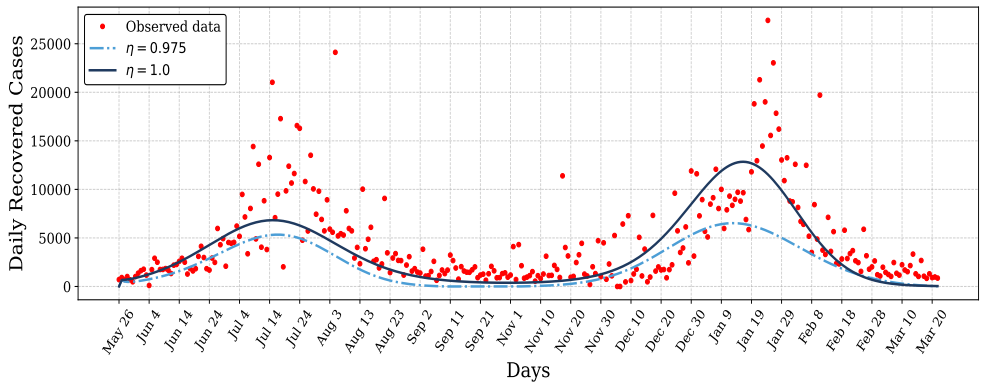

Figure 18. Model fit of daily recovered cases COVID-19 for different fractional derivative orders η, with parameters estimated for each value of η.

- **Immunity dynamics.** Waning immunity and reinfection are not modelled explicitly; over the roughly ten-month, two-wave horizon studied here this is a reasonable simplification, but it precludes multi-year projections.

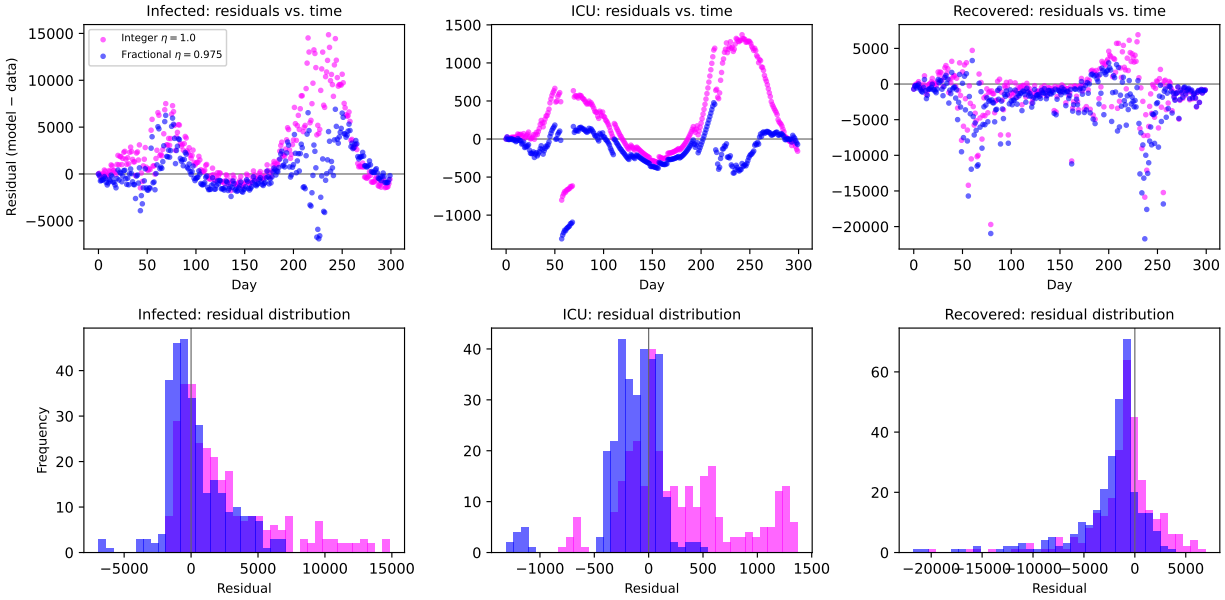

Figure 19. Residual diagnostics for the fractional ($\eta = 0.975$) and integer-order ($\eta = 1.0$) fits.

- **Surveillance and reporting biases.** The calibration relies on passive testing registries, which are subject to under-reporting and reporting delays, particularly during peak surges. The estimated removal rate δ should accordingly be read as an effective surveillance turnover rate rather than a purely clinical recovery rate.
- **Parameter identifiability.** With only three observed compartments the full parameter set is weakly identifiable and several parameters are strongly correlated; in particular the recovery rate λ and the ICU mortality rate μ enter the observable dynamics only through the combination $\mu + \lambda$ and cannot be estimated separately. The reported confidence intervals for the epidemiological rates are therefore conditional on the fitted transmission timeline $\beta(t)$, and the individual values of λ and μ should be regarded as indicative rather than precisely determined; the disease-induced mortality rate μ is especially weakly constrained because the deceased compartment D is not observed. In the same vein, the profile analysis of Figure 15 shows that the data do not sharply distinguish the fractional order $\eta = 0.975$ from the integer value $\eta = 1$, so the fractional order should be viewed as a well-fitting and physically interpretable modelling choice rather than a uniquely identified quantity.
- **Scope of the validation.** The out-of-sample assessment is a random hold-out and is therefore interpolative: it guards against in-sample over-fitting but does not establish forward-forecasting skill, which—as a temporal hold-out indicates—is considerably harder for an unseen epidemic wave whose intervention timeline is not represented in the training data.

9. Conclusions

In this study, we proposed a fractional-order SEICRD model with a time-dependent infectious communication rate $\beta(t)$, formulated using the Caputo fractional derivative, to describe the COVID-19 dynamics in South Africa over two epidemic waves. The model incorporates memory effects through the fractional-order parameter and accounts for non-pharmaceutical interventions using the Woods–Saxon function. The model accurately fits the reported daily infected, daily recovered cases and ICU cases from 26 May 2020 to 20 March 2021, which leads to an optimal estimate of the epidemiological parameters of the model in both waves in South Africa, (Table 2). To identify the parameters that have the greatest influence on the dynamics of infected individuals and ICU cases during the two

waves, sensitivity analyses were performed for selected model parameters, namely the effective transmission rate γ, The estimated duration or illness δ, and the infectious communication rate β_0. The computed sensitivity indices, quantify the relative impact of these parameters on the disease dynamics.
Figures 7, 8 and 9 and 10 , 11, 12 and 13, 14 show the sensitivity of the infected population dynamics to changes on the parameters γ, λ, α and β_0, respectively. By comparing the effects of these parameters on the infected population dynamics through the figures, we find that the dynamics of the model is more sensitive to the change in parameter β_0, followed by γ. Furthermore, the parameter α exerts a greater influence on the dynamics of infected population at the ICU than λ. Notably, the two parameters with the most significant impact,β_0 and γ, are directly related to the basic reproduction number $\mathcal{R}_0$.
.

From these results, we conclude that reducing the effective transmission rate and the infectious communication rate significantly decreases the number of infected individuals and delays the epidemic peak. This delay leads to a reduction in the peak burden on the healthcare system, particularly ICU demand. The findings suggest that early and effective implementation of non-pharmaceutical interventions, such as lockdowns, social distancing, and restrictions on contact rates, plays a crucial role in controlling the spread of COVID-19. Overall, the study demonstrates that decreasing the infection transition rate between individuals has a substantial positive effect in limiting COVID-19 transmission in South Africa, and that the fractional-order formulation provides a more realistic description of epidemic dynamics by capturing the long-term memory effects observed across successive epidemic waves.

Beyond the sensitivity results, a comparison against the integer-order model ($\eta = 1$) showed that the fractional formulation fits the observed infected and ICU compartments at least as well while parsimoniously encoding memory effects (Table 4); a profile analysis (Figure 15) further showed that the fractional order is only weakly identified, so it is presented as a physically interpretable modelling choice rather than a decisively selected value. Residual diagnostics (Figure 19) and a random hold-out test indicate that the fit reflects genuine descriptive adequacy rather than in-sample overfitting. Practically, integrating the fitted ICU trajectories over the two waves suggests that the memory-driven attenuation corresponds to approximately $125{,}000$ fewer ICU bed-days than the integer-order projection, underscoring the operational relevance of early, well-timed non-pharmaceutical interventions for preserving health-system capacity. These conclusions should nonetheless be read in light of the modelling assumptions discussed in Section 8—notably homogeneous mixing, simplified immunity dynamics, and reliance on surveillance data—which also delineate natural directions for future work, including age- or region-structured extensions and validation against independent seroprevalence and excess-mortality estimates.

Data and Code Availability

The observational data used for calibration (South African daily infected, ICU, and recovered series, 26 May 2020–20 March 2021) are contained in the file `stacked_solutions_and_data_3.csv`. The complete source code that reproduces the revised results—the fractional Adams–Bashforth–Moulton solver, the parameter estimation and conditional confidence intervals, the profile analysis of the fractional order, the peak-sensitivity table, the intervention-timing scenario, and the vital-dynamics assessment—is provided as supplementary material and is available from the corresponding author on request.

REFERENCES

1. World Health Organization (WHO), *Coronavirus disease (COVID-19) situation reports and data*, https://apps.who.int/iris/handle/10665/331221, 2020.
2. WHO, *WHO. Middle East respiratory syndrome coronavirus (MERS-CoV).* *https://www.who.int/csr/disease/coronavirus-infections/ar/*.
3. World Health Organization (WHO), "Coronavirus disease (COVID-19) pandemic," Available at: https://www.who.int/emergencies/diseases/novel-coronavirus-2019, [Accessed: January 22, 2021].
4. Coronavirus 2019, *Symptoms of Coronavirus. CDC,* *https://www.cdc.gov/coronavirus/2019-ncov/symptoms-testing/symptoms.html*.

5. Coronavirus 2019, *Social Distancing, Quarantine, and Isolation-CDC*, https://www.cdc.gov/coronavirus/2019-ncov/prevent-getting-sick/social-distancing.html.
6. N.H. Tuan, H. Mohammadi, S. Rezapour, *A mathematical model for COVID-19 transmission by using the Caputo fractional derivative*, Chaos, Solitons & Fractals, vol. 140, pp. 110107, 2020.
7. S. Ahmad, A. Ullah, Q.M. Al-Mdallal, H. Khan, K. Shah, A. Khan, *Fractional order mathematical modeling of COVID-19 transmission*, Chaos, Solitons & Fractals, vol. 139, pp. 110256, 2020.
8. Fatmawati, E. Yuliani, C. Alfiniyah, M.L. Juga, C.W. Chukwu, *On the modeling of COVID-19 transmission dynamics with two strains: insight through Caputo fractional derivative*, Fractal and Fractional, vol. 6, no. 7, pp. 346, 2022.
9. F. Ndaïrou, I. Area, J.J. Nieto, C.J. Silva, D.F.M. Torres, *Fractional model of COVID-19 applied to Galicia, Spain and Portugal*, Chaos, Solitons & Fractals, vol. 144, pp. 110652, 2021.
10. I.G. Ameen, H.M. Ali, M.R. Alharthi, A.-H. Abdel-Aty, H.M. Elshehabey, *Investigation of the dynamics of COVID-19 with a fractional mathematical model: A comparative study with actual data*, Results in Physics, vol. 23, pp. 103976, 2021.
11. G.-C. Wu, J.-L. Wei, C. Luo, L.-L. Huang, *Parameter estimation of fractional uncertain differential equations via Adams method*, Nonlinear Analysis: Modelling and Control, vol. 27, no. 3, pp. 413–427, 2022.
12. Y. Chen, F. Liu, Q. Yu, T. Li, *Review of fractional epidemic models*, Applied Mathematical Modelling, vol. 97, pp. 281–307, 2021.
13. A. Atangana, *Modelling the spread of COVID-19 with new fractal-fractional operators: can the lockdown save mankind before vaccination?*, Chaos, Solitons & Fractals, vol. 136, pp. 109860, 2020.
14. M. Ali, M. Bakheet, E. Bashier, *A mathematical model for non-pharmaceutical interventions in the transmission of Covid-19*, J. Math. Comput. Sci., vol. 12, pp. Article–ID, 2022.
15. A. A. Kilbas, O. I. Marichev, and S. G. Samko, *Fractional integrals and derivatives (theory and applications)*, Gordon and Breach, Switzerland, 1993.
16. H. Jafari,Bashforth Moulton C. M. Khalique, and M. Nazari, *Application of the Laplace decomposition method for solving linear and nonlinear fractional diffusion–wave equations*, Applied Mathematics Letters, vol. 24, no. 11, pp. 1799–1805, 2011.
17. A. A. Kilbas, H. M. Srivastava, and J. J. Trujillo, *Theory and applications of fractional differential equations*, Elsevier, vol. 204, 2006.
18. P. J. Collins, *Differential and integral equations*, OUP Oxford, 2006.
19. Ayoub, Houssein H and Chemaitelly, Hiam and Mumtaz, Ghina R and Seedat, Shaheen and Awad, Susanne F and Makhoul, Monia and Abu-Raddad, Laith J, *Characterizing key attributes of COVID-19 transmission dynamics in China's original outbreak: Model-based estimations*, Elsevier Journal of Global epidemiology, 2020.
20. P. van den Driessche and J. Watmough, *Reproduction numbers and sub-threshold endemic equilibria for compartmental models of disease transmission*, Mathematical Biosciences, vol. 180, no. 1–2, pp. 29–48, 2002.
21. Choghadi, M. A. and Talebi, H. A., *The Routh-Hurwitz stability criterion, revisited: The case of multiple poles on imaginary axis*, IEEE Transactions on Automatic Control, vol. 58, no. 3, pp. 750–755, 2013.
22. C. Li and C. Tao, *On the fractional Adams method*, Computers & Mathematics with Applications, vol. 58, no. 8, pp. 1573–1588, 2009.
23. Korolev, and Ivan, *Identification and estimation of the SEIRD epidemic model for COVID-19*, Elsevier Journal of econometrics, vol. 220, no. 1, pp. 63–85, 2021.
24. Trisilowati, I., Darti, I., Musafir, R. R., Rayungsari, M., and Suryanto, A., *Dynamics of a fractional-order COVID-19 epidemic model with quarantine and standard incidence rate*, Axioms, vol. 12, no. 6, p. 591, 2023.
25. Y. Qiao, Y. Ding, D. Pang, B. Wang, and T. Lu, *Fractional-Order Modeling of COVID-19 Transmission Dynamics: A Study on Vaccine Immunization Failure*, Mathematics, vol. 12, no. 21, p. 3378, 2024.
26. National Institute for Communicable Diseases (NICD), *National COVID-19 surveillance reports*, South Africa, 2020. https://www.nicd.ac.za.
27. Data Science for Social Impact Research Group (DSFSI), *COVID-19 South Africa data repository*, University of Pretoria, 2020. https://github.com/dsfsi/Covid19za.
28. South African COVID-19 Data Portal, *COVID-19 South Africa dashboard*, Online Repository, 2020. https://bitly.com/Covid19za-dash.
29. Statistics South Africa, *Mid-year population estimates 2020*, Statistical Release P0302, Pretoria, 2020.